

On the formation of H α line emission around classical T Tauri stars

Ryuichi Kurosawa^{1*}, Tim J. Harries¹ and Neil H. Symington²

¹*School of Physics, University of Exeter, Stocker Road, Exeter EX4 4QL.*

²*School of Physics and Astronomy, University of St. Andrews, North Haugh, St. Andrews, Fife, KY16 9SS.*

Dates to be inserted

ABSTRACT

We present radiative transfer models of the circumstellar environment of classical T Tauri stars, concentrating on the formation of the H α emission. The wide variety of line profiles seen in observations are indicative of both inflow and outflow, and we therefore employ a circumstellar structure that includes both magnetospheric accretion and a wind. We adopt two kinematic models for the outflow, a generic bipolar wind and a disc wind. We perform systematic investigations of the model parameters for the wind and the magnetosphere to search for possible geometrical and physical conditions which lead to the types of profiles seen in observations. We find that both wind models can reproduce the wide range profile types seen in observations, and that the most common profile types observed occupy a large volume of parameter space. Conversely, the most infrequently observed profile morphologies require a very specific set of models parameters. Although a particular outflow model (bipolar or disc-wind) is not well-constrained by a single line profile observations, we find that the inclination dependence of the line equivalent width predicted by the bipolar wind model agree with trends seen in the observation, but the disc-wind model does not. Using the model results, we examine the H α spectroscopic classification used by Reipurth et. al, and discuss the basic physical conditions that are required to reproduce the profiles in each classified type.

Key words: stars: formation – circumstellar matter – radiative transfer – stars: pre-main-sequence

1 INTRODUCTION

T Tauri stars (TTS) are young ($\gtrsim 3 \times 10^6$ yrs, Appenzeller & Mundt 1989) low-mass objects, and are the progenitors of solar-type stars. Classical T Tauri stars (CTTS) exhibit strong H α emission, and typically have spectral types of F–K. Some of the most active CTTS show emission in higher Balmer lines and metal lines (e.g., Ca II H and K). They also exhibit excess continuum flux in the ultraviolet (UV) and infrared (IR). Their spectral energy distribution and polarisation data suggest the presence of circumstellar discs, which plays an important role in regulating dynamics of gas flows around CTTS (e.g. Camenzind 1990).

Many observational studies (e.g., Herbig 1962; Edwards et al. 1994; Kenyon et al. 1994; Reipurth, Pedrosa, & Lago 1996; Alencar & Basri 2000) of CTTS line profiles have revealed evidence for both outward wind flows and inward accretion flows, characterised by the blue-shifted absorption features in H α profiles and the redshifted inverse P Cygni (IPC) profiles respectively. Typical mass-loss rates of CTTS are about $10^{-9} M_{\odot} \text{ yr}^{-1}$ to $10^{-7} M_{\odot} \text{ yr}^{-1}$ (e.g., Kuhi 1964; Edwards et al. 1987; Hartigan, Edwards, & Ghandour 1995), and the mass-accretion rates are also about $10^{-9} M_{\odot} \text{ yr}^{-1}$ to $10^{-7} M_{\odot} \text{ yr}^{-1}$ (e.g., Kenyon & Hart-

mann 1987; Bertout, Basri, & Bouvier 1988; Gullbring et al. 1998). Recent H α spectro-astrometric observations by Takami, Bailey, & Chrysostomou (2003) provide indirect evidence for the presence of bipolar and monopolar outflows down to ~ 1 au scale (e.g. CS Cha and RU Lup). Similarly, ESO VLT observations using high-resolution ($R = 50\,000$) two-dimensional spectra of edge-on CTTS (HH30*, HK Tau B, and HV Tau C) by Appenzeller et al. (2005) show extended H α emission in the direction perpendicular to the obscuring circumstellar disc, suggesting the presence of the bipolar outflows. On an even larger scale, *HST* observations of HH30 (Burrows et al. 1996) trace the jet to within $\lesssim 30$ au of the star. The jet has a cone shape with an opening angle of 3° between 70 and 700 au (Königl & Pudritz 2000). Alencar & Basri (2000) found about 80 per cent of their sample (30 CTTS) show blue-shifted absorption components in at least one of the Balmer lines and Ca K.

In the currently favoured model of accretion in CTTS, the accretion disc is disrupted by the magnetosphere, which channels the gas from the disc onto the stellar surface (e.g., Uchida & Shibata 1985; Königl 1991; Collier Cameron & Campbell 1993; Shu et al. 1994). This picture is supported by recent measurements of strong ($\sim 10^3$ G) magnetic fields in CTTS (e.g., Johns-Krull et al. 1999; Symington et al. 2005b) and by radiative transfer models which reproduce the gross characteristics of observed profiles for some

* E-mail:rk@astro.ex.ac.uk

CTS (Muzerolle, Calvet, & Hartmann 2001). In particular the magnetospheric accretion (MA) model explains blue-ward asymmetric emission line profiles as resulting from the partial occultation of the flow by the stellar photosphere, while inverse P Cygni profiles in the MA model result from inflowing material at near free-fall velocities seen projected against hotspots on the stellar surface.

Despite these successes, the overwhelming observational evidence for outflow in the CTS suggests that the MA model is only one component of a complex circumstellar environment. Clearly, one must include the contribution of any wind/jet flow if one wishes to both accurately predict the mass-accretion rate and also determined the mass-loss rate of CTS via emission profile modelling. The first attempt in this direction was made by Alencar et al. (2005) who demonstrated that the observed H α , H β and Na D lines of RW Aur are better reproduced by the radiative transfer model which included a collimated disc-wind arising from near the inner edge of the accretion disc.

The main aim of this paper is to find a simple kinematic model which can reproduce the wide variety of the observed profiles, and to perform empirical studies of line formation in an attempt to place morphological classification schemes on a firmer physical footing. We will also discuss whether our model is consistent with some predictions made by recent MHD studies i.e. $\mu = \dot{M}_{\text{wind}}/\dot{M}_{\text{acc}} \approx 0.1$ (e.g. Königl & Pudritz 2000).

In section 2, the model assumptions, and the basic model configurations are presented. We discuss the radiative transfer model used to compute the profiles in section 3, and the results of model calculations are given in section 4. We discuss our results in the context of Reipurth's classification scheme in section 5, and our summary and conclusions are presented in section 6.

2 MODEL CONFIGURATION

In order to understand how the different parts of the CTS circumstellar environment contribute to the formation of H α , the model space is divided into four different regions: (1) a central continuum source, (2) the magnetospheric accretion flow, (3) the wind outflow, and (4) the accretion disc. Fig. 1 depicts the relative location of the regions in the model space. The density is assumed to be rotationally symmetric around the z -axis. The innermost radius of the magnetosphere at the equatorial plane coincides with the inner radius of the accretion disc. From the innermost part of the accretion disc, the gas falls freely, moving along the magnetic field onto the surface of the star. In the following subsections we describe the details of model components.

2.1 The continuum source

We adopt stellar parameters of a typical classical T Tauri star for the central continuum source, i.e. radius (R_*), mass (M_*), and effective temperature the photosphere (T_{ph}) are $2 R_{\odot}$, $0.5 M_{\odot}$, and 4000 K respectively. The model atmosphere of Kurucz (1979) with $T_{\text{ph}} = 4000$ K and $\log g_* = 3.5$ (cgs) defines the photospheric contribution to the continuum flux. The parameters are summarised in Table 1.

An additional continuum source is considered for models which includes magnetospheric accretion: as the infalling gas approaches the stellar surface, it decelerates in a strong shock, and is heated to $\sim 10^6$ K. The X-ray radiation produced in the shock will be absorbed by the gas locally, and re-emitted in optical and UV radiation (Königl 1991; Hartmann, Hewett, & Calvet 1994). This will

create hot rings where the magnetic field intersects with the surface. We assume that the free-falling kinetic energy is thermalized in the radiating layer, and is re-emitted as blackbody radiation with a single temperature. With the parameters of the magnetosphere and the star given above (Table 1), about 8 per cent of the surface is covered by the hot rings. If the mass-accretion rate is $10^{-7} M_{\odot} \text{ yr}^{-1}$, the ratio of this accretion luminosity to the photospheric luminosity is about 0.5, and the corresponding temperature of the hot rings is about 6400 K. The continuum emission from the hot rings is taken into account when computing the line profiles.

2.2 The magnetosphere

We adopt the MA flow model of Hartmann et al. (1994), as done by Muzerolle et al. (2001) and by Symington, Harries, & Kurosawa (2005a), in which the gas accretion on to the stellar surface from the innermost part of the accretion disc occurs through a dipolar stellar magnetic field. The magnetic field is assumed to be so strong that the gas flow does not affect the underlying magnetic field itself. As shown in Fig. 1, the innermost radius (R_{mi}) of the magnetosphere at the equatorial plane ($z = 0$) is assigned to be same as the inner radius (R_{di}) of the accretion disc where the flow is truncated. In our models, R_{mi} and the outer radius (R_{mo}) of the magnetosphere (at the equatorial plane) are set to be $2.2 R_{\odot}$ and $3.0 R_{\odot}$ respectively. The geometry of the magnetic field/stream lines is fixed for all calculations. We note that this magnetospheric geometry is identical to the "small/wide" model of Muzerolle et al. (2001).

The magnetic field and the gas stream lines are assumed to have the following simple form:

$$r = R_m \sin^2 \theta \quad (1)$$

(see Ghosh, Pethick, & Lamb 1977) where r , and θ are coordinates of the field point (p) in Fig. 1 in spherical coordinates, and R_m is the radial distance to the field line at the equatorial plane ($\theta = \pi/2$). The range of R_m is restricted between R_{mi} and R_{mo} . Using the field geometry above and conservation of energy, the velocity and the density of the accreting gas along the stream line are found as in Hartmann et al. (1994).

The temperature structure of the magnetospheric used by Hartmann et al. (1994) is adopted here. They computed the temperature, assuming a volumetric heating rate which is proportional to r^{-3} , by solving the energy balance of the radiative cooling rate of Hartmann et al. (1982) and the heating rate (Hartmann et al. 1994). Martin (1996) presented a self-consistent determination of the thermal structure of the inflowing gas along the dipole magnetic field (equation 1) by solving the heat equation coupled to the rate equations for hydrogen. He found that main heat source is adiabatic compression due to the converging nature of the flow, and the major contributors to the cooling process are bremsstrahlung radiation and line emission from Ca II and Mg II ions. The results of Martin (1996) qualitatively agree with that of Hartmann et al. (1994).

2.3 Outflow geometries

The magneto-centrifugal wind paradigm, first proposed by Blandford & Payne (1982), has been often used to model the large-scale wind structure of T Tauri stars, or the observed optical jets (e.g. HH 30 jet by Burrows et al. 1996; Ray et al. 1996). The launching of the wind from a Keplerian disc is typically done by treating the equatorial plane of the disc as a mass-injecting boundary condition (e.g., Shu et al. 1994; Ustyugova et al. 1995; Ouyed

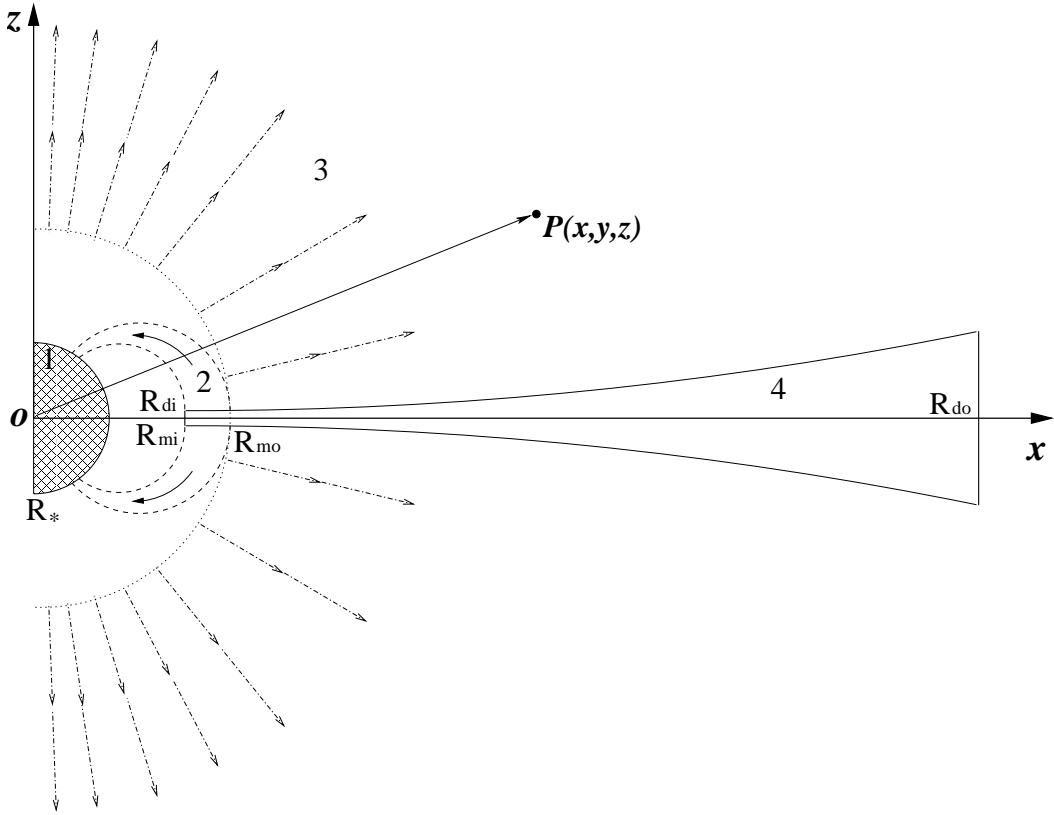


Figure 1. The basic model configuration. The system consists of four components: (1) the continuum source located at the origin (o) of the cartesian coordinates (x, y, z) – the y -axis is into the paper, (2) the magnetospheric accretion flow, (3) the bipolar wind outflow, and (4) the accretion disc. The density distribution is symmetric around the z -axis. The innermost radius of the magnetosphere (at the equatorial plane) coincides with the inner radius of the accretion disc. From the innermost part of the accretion disc, the gas falls freely, moving along the magnetic field onto the surface of the star. The bipolar wind starts from just outside the largest radius (R_{mo}) of the magnetosphere (dotted line).

Table 1. Summary of the standard classical T Tauri star model parameters.

Parameters	R_* [R_\odot]	M_* [M_\odot]	T_{ph} [K]	R_{mi} [R_*]	R_{mo} [R_*]	\dot{M}_{acc} [$M_\odot \text{ yr}^{-1}$]	\dot{M}_{wind} [$M_\odot \text{ yr}^{-1}$]	v_∞ [km s^{-1}]	b [–]	R_{di} [R_*]	R_{do} [au]
Standard	2.0	0.5	4000	2.2	3.0	10^{-7}	10^{-8}	210	4.0	2.2	100

& Pudritz 1997; Krasnopol'sky et al. 2003). Depending on the location of the open magnetic fields anchored to the disc, two different types of winds are produced. If the field is constrained to be near the co-rotation radius of stellar magnetosphere, an “X-wind” (Shu et al. 1994) is produced. If the open field lines are located in a wider area of the disc, a “disc-wind” similar to that of Königl & Pudritz (2000) is produced (Krasnopol'sky et al. 2003). Recent reviews on the jet/wind-disc connection can be found in Königl & Pudritz (2000) and Pudritz & Banerjee (2005).

Clearly there are several alternative outflow scenarios. Here we adopt two simple kinematical models which broadly represent the results of MHD simulations. The first is a bipolar wind model, in which the outflow is collimated along the rotational axes (a model similar to that of Krasnopol'sky et al. (2003)). The second model is based on the disc-wind paradigm, in which the density of the outflow increases towards the equatorial plane. The difference in latitudinal density structure between the two outflow models should provide an indication as to whether line profiles alone

can be used to constrain the outflow geometry. In the following sections we present details of the two outflow structures.

2.3.1 The bipolar wind

In a similar fashion to the simple model of Appenzeller et al. (2005), the following parametrisation of collimated bipolar wind (region 3 in Fig. 1) is adopted. The wind velocity field, \mathbf{v}_{wind} , consists of radial and azimuthal components which depend on the spherical coordinates r and θ . The radial component $v_r(r)$ is assumed to follow the classical beta-velocity law (c.f. Castor & Lamers 1979), and the azimuthal component v_ϕ is assumed to be a constant fraction (γ) of the Keplerian velocity for a given distance ($w = \sqrt{x^2 + y^2}$) from the symmetry axis (z -axis), i.e.:

$$\mathbf{v}_{\text{wind}} = v_r \hat{\mathbf{r}} + v_\phi \hat{\phi} \quad (2)$$

where

$$v_r(r) = v_{r0} + (v_\infty - v_{r0}) \left(1 - \frac{R_{\text{mo}}}{r}\right)^\beta, \quad (3)$$

and

$$v_\phi(w) = \gamma \left(\frac{GM_*}{w} \right)^{1/2}. \quad (4)$$

Note that the base of the wind starts at $r = R_{\text{mo}}$. This naturally leads to a density discontinuity, but allows a simple parameterisation of the wind whereas a self-consistent interface between the magnetosphere and wind would require a full MHD calculation that is beyond the scope of this paper. The range of polar angle for the wind is restricted to $\theta > |\theta_{\text{disc}}|$ where θ_{disc} is the opening angle of the accretion disc. v_{r0} is the small radial velocity at the base of the wind ($r = R_{\text{mo}}$). Normally, $v_{r0} = 10 \text{ km s}^{-1}$ which is approximately equal to the thermal velocity of hydrogen with $T = 7500 \text{ K}$. Following Appenzeller et al. (2005), $\gamma = 0.05$ is adopted. The dependency of v_r in polar direction ($\theta = 0$) on the values of wind acceleration parameter β is shown in Figure 2. All other parameters describing the wind are fixed as the standard values given in Table 1.

The density of the wind is assumed to be axi-symmetric and separable in r and θ ,

$$\rho(r, \theta) = P(r) F(\theta) \quad (5)$$

with

$$F(\theta) = n \cos^b \theta \quad (6)$$

where b is normally a positive even number (for density symmetric about the equatorial plane), and n is the angular normalisation constant. For $b = 0$, the wind is spherically symmetric except for the parts disrupted by the accretion disc. The larger the value of b , the higher the degree of the collimation. By integrating equation 6 over angles and normalising the integral to 4π , one finds

$$n = \frac{1+b}{1 - \cos^{1+b} \theta_{\text{wind}}}. \quad (7)$$

Assuming the total mass-loss rate via the wind is \dot{M}_{wind} and the mass-flux is constant, the radial part of the density function is reduced to $P(r) = \dot{M}_{\text{wind}} [4\pi r^2 v_r(r)]^{-1}$; hence, equation 5 becomes

$$\rho(r, \theta) = \frac{n \dot{M}_{\text{wind}} \cos^b \theta}{4\pi r^2 v_r(r)}. \quad (8)$$

For a given mass-accretion rate, the wind mass-loss rate in our typical model is assigned from the ratio of mass-loss to mass-accretion rate $\dot{M}_{\text{wind}}/\dot{M}_{\text{acc}} \approx 0.1$, a value indicated by both observations and MHD calculations (e.g. Königl & Pudritz 2000). Figure 2 shows the density along a streamline in the polar direction ($\theta = 0$), for different values of β with all other parameters fixed at the standard values (Table 1). The density is relatively sensitive to the value of β for $r < 10 R_{\text{mo}}$.

2.3.2 The disc wind

Knigge, Woods, & Drew (1995) introduced the ‘‘split-monopole’’ kinematic disc-wind model in their studies of the UV resonance lines formed in the winds of cataclysmic variable stars. His formalism provides a simple parameterisation of a disc wind that has similar properties to those found by MHD modelling. In this model, the outflow arises from the surface of the rotating accretion disc, and

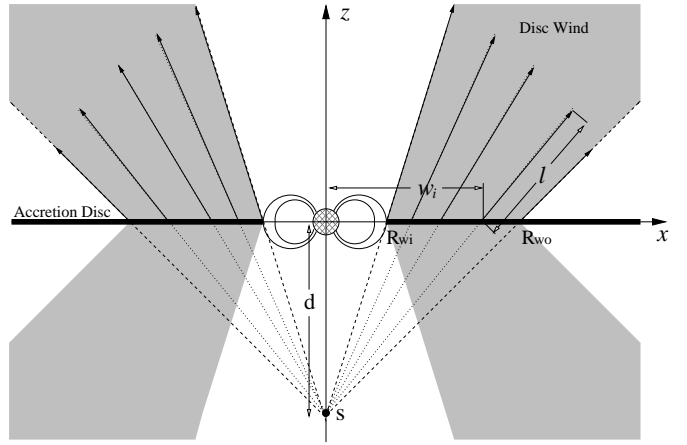


Figure 3. Basic model configuration of the disc-wind, magnetosphere hybrid model. The system consists of four components: (1) the continuum source located at the origin (o) of the cartesian coordinates (x, y, z) – the y -axis is into the paper, (2) the magnetospheric accretion flow, (3) the disc wind, and (4) the geometrically thin (but opaque) accretion disc. The disc wind originates from the disc surface between $w_i = R_{wi}$ and $w_i = R_{wo}$. The wind source points (S), from which the stream lines diverge, are placed at distance d above and below the star. The degree of wind collimation is controlled by changing the value of d .

has a biconical geometry. The specific angular momentum is assumed to be conserved along a stream line, and the poloidal velocity component is assumed to be simply a radial from vertically displaced ‘‘sources’’ from the central star. Here we briefly describe the disc-wind model, and readers are referred to Knigge et al. (1995) and Long & Knigge (2002) for details.

The four basic parameters of the model are: (1) the mass-loss rate, (2) the degree of the wind collimation, (3) the velocity gradient, and (4) the wind temperature. The basic configuration of the disc-wind model is shown in Figure 3. The disc wind originates from the disc surface, but the ‘‘source’’ point (S), from which the stream lines diverge, are placed at distance d above and below the centre of the star. The angle of the mass-loss launching from the disc is controlled by changing the value of d . The mass-loss launching occurs between R_{wi} and R_{wo} where the former is set to be equal to the outer radius of the magnetosphere (R_{mo}) and the latter is set to 1 au as in Krasnopol'sky et al. 2003.

The local mass-loss rate per unit area (\dot{m}) is assumed to be proportional to the mid-plane temperature of the disc, and is a function of the cylindrical radius $w = (x^2 + y^2)^{1/2}$, i.e.

$$\dot{m}(w) \propto T(w)^\alpha. \quad (9)$$

The mid-plane temperature of the disc is assumed to be expressed as a power-law in w ; thus, $T \propto w^q$. Using this in the relation above, one finds

$$\dot{m}(w) \propto w^p \quad (10)$$

where $p = \alpha \times q$. The index of the mid-plane temperature power law is adopted from the dust radiative transfer model of Whitney et al. (2003) who found the innermost part of the accretion disc has $q = -1.15$. In order to be consistent with the collimated disc-wind model of Krasnopol'sky et al. (2003) who used $p = -3/2$, the value of α is set to 1.3. The constant of proportionality in equation 10 is found by integrating \dot{m} from R_{wi} to R_{wo} , and the normalising the value to the total mass-loss rate \dot{M}_{dw} .

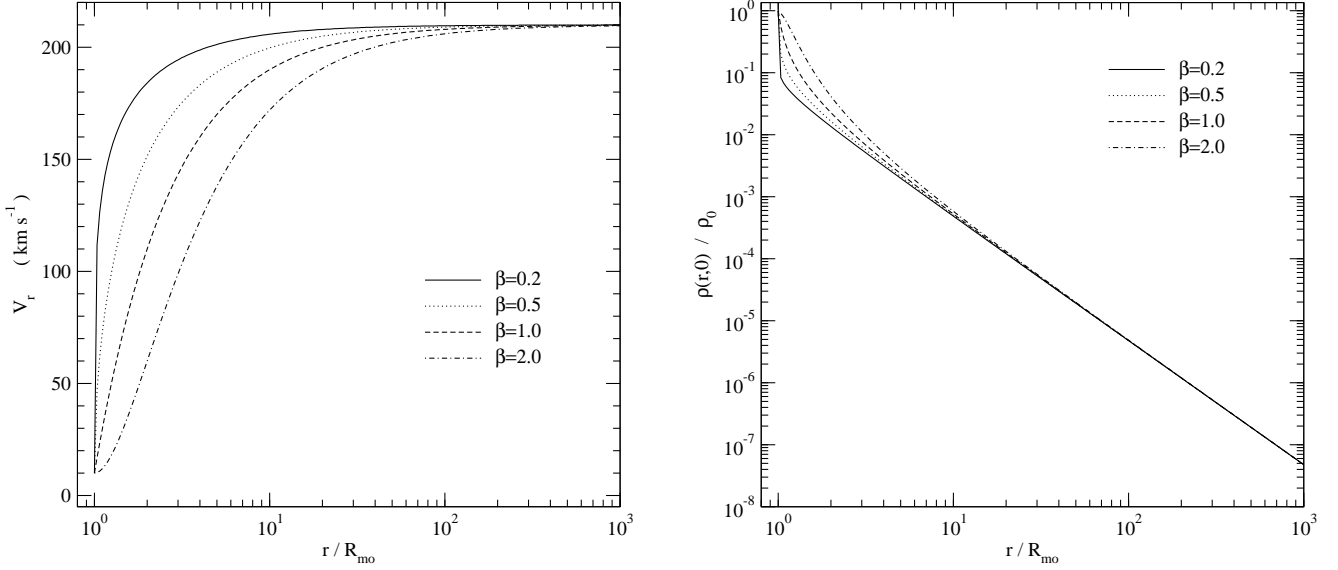


Figure 2. The dependency of the bipolar wind velocity and density structure on the wind acceleration parameter β . The radial component of the wind velocity (equation 3) in polar direction, $\theta = 0$ as a function of radius is shown on the left. The wind density (equation 8 along polar direction as a function of radius is shown on the right. For all β values, the density is normalised to the density at the base of the wind in polar direction, i.e. $\rho_0 = \rho(R_{\text{mo}}, 0)$. The smaller the value of β , the faster the acceleration of the wind. For the radii $r/R_{\text{mo}} < 10$, both velocity and density are sensitive to the value of β . For all β values, the radial velocity of the wind reaches the terminal velocity ($\sim 210 \text{ km s}^{-1}$) by $r/R_{\text{mo}} \sim 1000$. The initial velocity $V_0 = 10 \text{ km s}^{-1}$, which approximately corresponds to the thermal velocity of a hydrogen atom at 7500 K, is used for all v_r plots.

The azimuthal/rotational component of the wind velocity $v_\phi(w, z)$ is computed from the Keplerian rotational velocity at the emerging point of the stream line i.e. $v_\phi(w_i, 0) = (GM_*/w_i)^{1/2}$ where w_i is the distance from the rotational axis (z) to the emerging point on the disc, and by assuming the conservation of the specific angular momentum along a stream line:

$$v_\phi(w, z) = v_\phi(w_i, 0) \left(\frac{w_i}{w} \right). \quad (11)$$

Based on the canonical β velocity law of hot stellar winds (c.f. Castor, Abbott, & Klein 1975), the poloidal component of the wind velocity (v_p) parameterised as:

$$v_p(w_i, l) = c_s(w_i) + [f v_{\text{esc}} - c_s(w_i)] \left(1 - \frac{R_s}{l + R_s} \right)^\beta \quad (12)$$

where c_s , f , and l are the sound speed at the wind launching point on the disc, the constant scale factor of the asymptotic terminal velocity to the local escape velocity (from the wind emerging point on the disc), and the distance from the disc surface along stream lines respectively. R_s is the wind scale length ($= 10 R_{\text{mi}}$, Long & Knigge 2002).

Assuming mass-flux conservation and using the velocity field defined above, the disc wind density as a function of w and l can be written as

$$\rho(w_i, l) = \frac{\dot{m}(w_i)}{v_p(w_i, l) |\cos \delta|} \left\{ \frac{d}{Q(w_i, l) \cos \delta} \right\}^2 \quad (13)$$

where Q and δ are the distance from the source point (S) to a point along the stream line and the angle between the stream line and the disc normal respectively. Figure 4 shows the density and the velocity components along the mid stream line (passing through $w_i = (R_{\text{wi}} + R_{\text{wo}})/2$ on the disc plane ($z = 0$) for different values of the wind acceleration parameter β .

2.4 The accretion disc

We adopt a simple analytical accretion disc model, the α -disc ‘standard model’ (Shakura & Sunyaev 1973; Frank, King, & Raine 2002) with the inner radius fixed at the inner radius of the magnetosphere at equatorial plane. This corresponds to Region 4 in Fig. 1.

2.4.1 Density and velocity

The disc density distribution is given by

$$\rho_d(w, z) = \Sigma(w) \frac{1}{\sqrt{2\pi} h(w)} e^{-\left(\frac{z}{2h(w)}\right)^2} \quad (14)$$

where $w = \sqrt{x^2 + y^2}$, h , z and Σ are the distance from the symmetry axis, the scale height, the distance from the disc plane, and the surface density at the mid-plane, respectively. The mid-plane surface density and the scale height are given as:

$$\Sigma(w) = \frac{5M_d}{8\pi R_{\text{do}}^2} w^{-3/4} \quad (15)$$

where R_{do} and M_d are the disc radius and the disc mass respectively.

$$h(w) = 0.05 R_{\text{do}} w^{9/8}. \quad (16)$$

With these parameters, the disc is slightly flared. The inner radius of the disc is set to $R_{\text{di}} = R_{\text{mi}}$. The disc mass, M_d , is assumed to be 1/100 of the stellar mass (M_*), and the outer disc radius (R_{di}) is 100 au. The velocity of the gas/dust in the disc is assumed to be Keplerian.

2.4.2 Dust model

In order to calculate the dust scattering and absorption cross section as a function of wavelength, the optical constants of Draine &

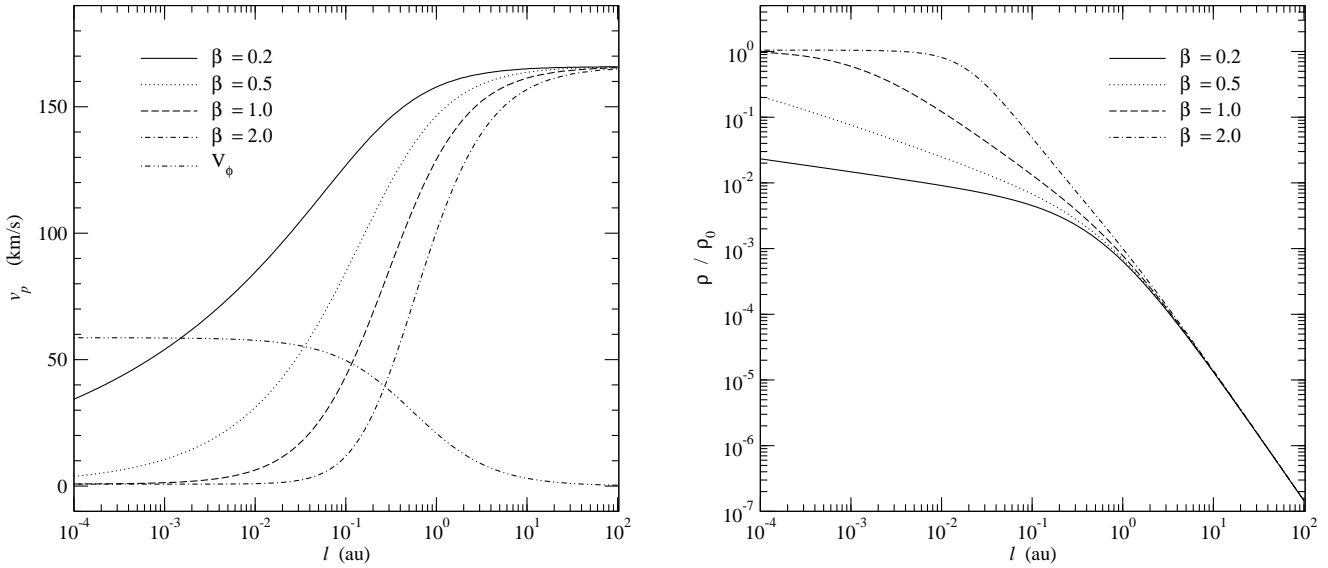


Figure 4. The dependency of the disc-wind density and velocity on the wind acceleration parameter β . The wind density ρ (left panel) and the poloidal velocity component v_p (right panel) along the stream line starting from the mid point of the wind launching zone, i.e. $(w, z) = (w_{\text{mid}}, 0)$ where $w_{\text{mid}} = (R_{\text{wi}} + R_{\text{wo}})/2$, are shown as a function of the distance (l) from the wind launching point (c.f. equations 12 and 13). The azimuthal velocity component (v_ϕ), which is independent of β (c.f. equation 11), is also shown in the right panel for comparison. The density is normalised to the density ρ_0 at the wind launching point for the $\beta = 1.0$ case. The v_p reaches the terminal velocity by 100 au for all β . In the far field ($l > 10$ au), the density is approximately proportional to $\sim l^2$.

Lee (1984) for amorphous carbon grains and Hanner (1988) for silicate grains are used. The model uses the “large grain” dust model of Wood et al. (2002) in which the dust grain size distribution is described by the following function:

$$n(a) da = (C_C + C_{\text{Si}}) a^{-p} \exp \left[-\left(\frac{a}{a_c} \right)^q \right] da \quad (17)$$

where a is the grain size restricted between a_{min} and a_{max} , and C_C and C_{Si} are the terms set by requiring the grains to completely deplete a solar abundance carbon and silicon. The parameters adopted in our model are: $C_C = 1.32 \times 10^{-17}$, $C_{\text{Si}} = 1.05 \times 10^{-17}$, $p = 3.0$, $q = 0.6$, $a_{\text{min}} = 0.1 \mu\text{m}$, $a_{\text{max}} = 1000 \mu\text{m}$, and $a_c = 50 \mu\text{m}$. This corresponds to Model 1 of the dust model used by Wood et al. (2002). See also their Fig. 3. The relative numbers of each grain is assumed to be that of solar abundance, $\text{C/H} \sim 3.5 \times 10^{-4}$ (Anders & Grevesse 1989) and $\text{Si/H} \sim 3.6 \times 10^{-5}$ (Grevesse & Noels 1993) which are similar to values found in the ISM model of Mathis, Rumpl, & Nordsieck (1977) and Kim, Martin, & Hendry (1994).

3 THE RADIATIVE TRANSFER MODEL

We have extended the TORUS radiative transfer code (Harries 2000; Kurosawa et al. 2004; Symington et al. 2005a) to include the multiple circumstellar components described above. In previous calculations (Symington et al. 2005a), the model was used with a three-dimensional (3-D) adaptive mesh refinement (AMR) grid to investigate the line variability associated with rotational modulation of complex geometrical configurations of magnetosospheric inflow (see also Kurosawa, Harries, & Symington 2005). We modified the code to handle the a two-dimensional (2-D) density distribution, and restricted our models to be axi-symmetric. Note that the velocity field is still in 3-D – the third component can be calculated by using symmetry for a given value of azimuthal angle.

The computation of $\text{H}\alpha$ is divided in two parts: (1) the source function calculation (S_ν) and (2) the observed flux/profile calculation. In the first process, we have used the method of Klein & Castor (1978) (see also Rybicki & Hummer 1978; Hartmann et al. 1994) in which the Sobolev approximation method is applied. The population of the bound states of hydrogen are assumed to be in statistical equilibrium, and the gas to be in radiative equilibrium. Our hydrogen atom model consist of 14 bound states and a continuum. Readers are refer to Harries (2000) for details.

Monte Carlo radiative transfer (e.g. Hillier 1991), under the Sobolev approximation, can be used when (1) a large velocity gradient is present in the gas flow, and (2) the intrinsic line width is negligible compared to the Doppler broadening of the line. In our earlier models (Harries 2000; Symington et al. 2005a), this method was adopted since these conditions are satisfied. However, as noted and demonstrated by Muzerolle et al. (2001), even with a moderate mass-accretion rate ($10^{-7} \text{ M}_\odot \text{ yr}^{-1}$), Stark broadening becomes important in the optically thick $\text{H}\alpha$ line. Muzerolle et al. (2001) also pointed out that the observed $\text{H}\alpha$ profiles from CTTS typically have the wings extending to 500 km s^{-1} (e.g. Edwards et al. 1994; Reipurth et al. 1996) which cannot be explained by the infall velocity alone.

We have implemented the broadening mechanism following the formalism described by Muzerolle et al. (2001). First, the emission and absorption profiles are replaced from the Doppler to the Voigt profile, which is defined as:

$$H(a, y) \equiv \frac{a}{\pi} \int_{-\infty}^{\infty} \frac{e^{-y'^2}}{(y - y')^2 + a^2} dy' \quad (18)$$

where $a = \Gamma/4\pi\Delta\nu_D$, $y = (\nu - \nu_0)/\Delta\nu_D$, and $y' = (\nu' - \nu_0)/\Delta\nu_D$ (c.f. Mihalas 1978). ν_0 is the line centre frequency, and $\Delta\nu_D$ is the Doppler line width of hydrogen atom (due to its thermal motion) which is given by $\Delta\nu_D = (2kT/m_H)^{1/2} \times (\nu_0/c)$ where m_H is the mass of a hydrogen atom. The damping

constant Γ , which depends on the physical condition of the gas, is parameterised by Vernazza, Avrett, & Loeser (1973) as follows:

$$\begin{aligned} \Gamma = & C_{\text{rad}} + C_{\text{vdW}} \left(\frac{n_{\text{HI}}}{10^{16} \text{ cm}^{-3}} \right) \left(\frac{T}{5000 \text{ K}} \right)^{0.3} \\ & + C_{\text{Stark}} \left(\frac{n_e}{10^{12} \text{ cm}^{-3}} \right)^{2/3} \end{aligned} \quad (19)$$

where n_{HI} and n_e are the number density of neutral hydrogens and that of free electrons. Also, C_{rad} , C_{vdW} and C_{Stark} are natural broadening, van der Waals broadening, and linear Stark broadening constants respectively. We simply adopt this parameterisation along with the values of broadening constants for H α from Luttermoser & Johnson (1992), i.e. $C_{\text{rad}} = 6.5 \times 10^{-4}$ Å, $C_{\text{vdW}} = 4.4 \times 10^{-4}$ Å and $C_{\text{Stark}} = 1.17 \times 10^{-3}$ Å. In terms of level populations and the Voigt profile, the line opacity for the transition $i \rightarrow j$ can be written as:

$$\chi_{ij} = \frac{\pi^{1/2} e^2}{m_e} f_{ij} n_j \left(1 - \frac{g_j n_i}{g_i n_j} \right) H(a, y) \quad (20)$$

where f_{ij} , n_i , n_j , g_i and g_j are the oscillator strength, the population of i -th level, the population of j -th level, the degeneracy of the i -th level, and the degeneracy of the j -th level respectively. m_e and e are the electron mass and charge (c.f. Mihalas 1978).

We further modified TORUS by replacing the Monte Carlo line transfer algorithm with a direct integration method (c.f. Mihalas 1978) for computing the observed flux as a function of frequency. The integration of the flux is performed in the cylindrical coordinate system (p, q, t) which is obtained by rotating the original stellar coordinate system (ρ, ϕ, z) around the y axis by the inclination of the line of sight. Note that the t -axis coincides with the line of sight with this rotation. The observed flux (F_ν) is given by:

$$F_\nu = \frac{1}{4\pi d^2} \int_0^{p_{\text{max}}} \int_0^{2\pi} p \sin q I_\nu \, dq \, dp \quad (21)$$

where d , p_{max} , and I_ν are the distance to an observer, the maximum extent to the model space in the projected (rotated) plane, and the specific intensity (I_ν) in the direction on observer at the outer boundary. For a given ray along t , the specific intensity is given by:

$$I_\nu = I_0 e^{-\tau_\infty} + \int_{t_0}^{t_\infty} S_\nu(t) e^{-\tau} dt \quad (22)$$

where I_0 and S_ν are the intensity at the boundary on the opposite to the observer and the source function (η_ν / χ_ν) of the stellar atmosphere/wind at a frequency ν . For a ray which intersects with the stellar core, I_0 is computed from the stellar atmosphere model of Kurucz (1979) as described in section 2.1, and $I_0 = 0$ otherwise. If the the ray intersects with the hot ring on the stellar surface created by the accretion stream, we set $I_0 = B_\nu(T_{\text{ring}})$ where B_ν is the Planck function and T_{ring} is the temperature of the hot ring. The initial position of each ray is assigned to be at the centre of the surface element ($dA = p \sin q \, dq \, dp$). The code execution time is proportional to $n_p n_q n_\nu$ where n_p and n_q are the number of cylindrical radial and angular points for the flux integration, and n_ν is the number of frequency points. In the models presented in the following section. $n_p = 180$, $n_q = 100$, and $n_\nu = 101$ are used unless specified otherwise. A linearly spaced radial grid is used for the area where the ray intersects with magnetosphere, and a logarithmically spaced grid is used for the wind and the accretion disc regions.

The optical depth τ is equation 22 is defined as:

$$\tau(t) \equiv \int_t^\infty \chi_\nu(t') dt'$$

where χ_ν is the opacity of media the ray passes through. τ_∞ is the total optical depth measured from the initial ray point to the observer (or to the outer boundary closer to the observer). Initially, the optical depth segments $d\tau$ are computed at the intersections of a ray with the original AMR grid in which the opacity and emissivity information are stored. For high optical depth models, additional points are inserted between the original points along the ray, and η_ν are χ_ν values are interpolated to those points to ensure $d\tau < 0.05$ for the all ray segments.

For a point in the magnetosphere and the wind flows, the emissivity and the opacity of the media are given as:

$$\begin{cases} \eta_\nu &= \eta_c^H + \eta_l^H \\ \chi_\nu &= \chi_c^H + \chi_l^H + \sigma_{\text{es}} \end{cases} \quad (23)$$

where η_c^H and η_l^H are the continuum and line emissivity of hydrogen. χ_c^H , χ_l^H , and σ_{es} are the continuum, line opacity (equation 20) of hydrogen, and the electron scattering opacity. Similarly, for a point in the accretion disc,

$$\begin{cases} \eta_\nu &= 0 \\ \chi_\nu &= \kappa_{\text{abs}}^{\text{dust}} + \kappa_{\text{sca}}^{\text{dust}} \end{cases} \quad (24)$$

where $\kappa_{\text{abs}}^{\text{dust}}$ and $\kappa_{\text{sca}}^{\text{dust}}$ are the dust absorption, and scattering opacity which are calculated using the dust property described in section 17. We neglect the emissivity from the disc: since the disc mass of CTTS are rather small ($\sim 0.01 M_\odot$) and low temperature ($< \sim 1600$ K), the continuum flux contribution at H α wavelength is expected to be negligible (e.g. Chiang & Goldreich 1997).

xxxx finished here xxxx

4 RESULTS

4.1 Magnetosphere

Using the standard parameters (Table 1) for the central star and the magnetosphere, we examine the dependency of H α on the temperature (T_{max}) of accretion flow and the mass accretion rate (\dot{M}_{acc}), as similarly done by Muzerolle et al. (2001) for H β . The hot ring temperature is computed from the available kinetic energy of the free-falling gas as describe by Hartmann et al. (1994) while Muzerolle et al. (2001) used the constant hot ring temperature (8000 K) for most of their models. The accretion luminosity (L_{acc}) of models with $\dot{M}_{\text{acc}} = 10^{-7} M_\odot \text{ yr}^{-1}$ is about a half of the total luminosity (without the hot ring) of the star, and L_{acc} is proportional to \dot{M}_{acc} . The results are placed in Figure 5. Overall dependency on T_{max} and \dot{M}_{acc} are similar to that of Muzerolle et al. (2001). In general, the line strength becomes weaker as the accretion rate and the temperature become smaller. The red-shifted absorption becomes less visible for higher accretion rate and temperature models in which the flux in the damping wings become important. Figure 6 shows an example of the effect of the broadening of H alpha (with $T_{\text{max}} = 7500$ K and $\dot{M}_{\text{acc}} = 10^{-7} M_\odot \text{ yr}^{-1}$) due to the damping constants as described in section 3. Although the maximum flux of the model with the broadening is almost identical to that of the model with no damping constant ($\Gamma = 0$), a significant increase of the line flux in both red and blue wings of seen in the model with broadening. The weak red-shifted absorption component (which is a signature of the magnetospheric accretion) is weakened or eliminated by the flux in broadened wing.

Table 2 shows the EW for the models shown in Figure 5. About a half of the models shown the figure agree with the observed EW values of H α from 30 TTS presented by Alencar &

Table 2. Summary of H α equivalent widths from the magnetospheric accretion flow models shown in Figure 5.

T_{\max} (K)	\dot{M}_{acc} ($M_{\odot} \text{ yr}^{-1}$)		
	10^{-7}	10^{-8}	10^{-9}
6500	17.9	0.1	0.0
7500	25.2	-0.9	-0.5
8500	68.3	6.5	-0.7
9500	98.6	52.4	1.3

Basri (2000) who found the EW of H α ranges from $\sim 3 \text{ \AA}$ to $\sim 160 \text{ \AA}$, and the mean to be $\sim 55 \text{ \AA}$. For the lowest \dot{M}_{acc} models, the EW values are smaller than the minimum EW observed by Alencar & Basri (2000), and for some models the EWs are negative. Since the target selection criteria of Alencar & Basri (2000) is not stated in their paper, we can not conclude that these low \dot{M}_{acc} models disagree with the observation. Reipurth et al. (1996), who measured the EW of 43 TTS and found similar distribution of EW values, mentioned that their EW measurements are under-representing real samples since the selection of the targets are based on the strong emission in H α surveys.

The dependency of the profile on the inclination angle (i) is demonstrated in Figure 7. The model uses the same parameters as in Figure 6 (with broadening, $T_{\max} = 7500 \text{ K}$ and $\dot{M}_{\text{acc}} = 10^{-7} M_{\odot} \text{ yr}^{-1}$). The figure shows that the peak (normalised) flux decreases as the inclination angle increases. Similarly, the equivalent width also decreases as the inclination increases. Because of the geometry of the magnetospheric accretion (c.f. Figure 1) and of the presence of the gas with the highest velocity close to the stellar surface, the highest red-shifted line-of-sight velocity is visible only at the high inclination angles. This explains the wider appearance of the profile with $i = 80^{\circ}$ compared to the relatively narrow line appearance of the profile with $i = 10^{\circ}$. Although not shown here, a similar dependency on the inclination angle is found for the models with different temperatures ($T_{\max} = 6500, 8500, 9500 \text{ K}$).

As seen in the models of Hartmann et al. (1994) and Muzerolle et al. (2001), our models also show the blue-shifted peak and the blue-ward asymmetry caused by the occultation of the accretion flow by the equatorial disc and the stellar disc. However, Alencar & Basri 2000 (see their Fig. 9) found a substantial fraction of the observed H α profiles also shows the ‘‘red-shifted’’ peak, and the P Cygni profiles which can not be explained by the magnetospheric accretion model alone. In addition, a recent study by Appenzeller et al. (2005) showed that the equivalent width of H α from CTTS increases as the inclination angle increases. Our model with the magnetospheric accretion flow clearly disagrees with their finding.

4.2 Bipolar Wind

As mentioned earlier, the magnetospheric accretion flow model alone cannot explain some of the features seen in observations. As an alternative model, we now examine formation of H α in a simple bipolar wind as described in section 2.3.1. The basic wind model parameters introduced earlier are γ , β , v_{∞} , b , θ_{wind} , T_{wind} and \dot{M}_{wind} . To minimise the number of free parameters, we initially adopt $\gamma = 0.05$, $v_{\infty} = 210 \text{ km s}^{-1}$ (Appenzeller et al. 2005) and $\dot{M}_{\text{wind}} = 10^{-8} M_{\odot} \text{ yr}^{-1}$. Further, the angular extent of the wind (the opening angle of the wind) is assumed to be $\theta_{\text{wind}} = 80^{\circ}$. The degree of collimation is initially chosen to be $b = 4$, i.e. the ratio of

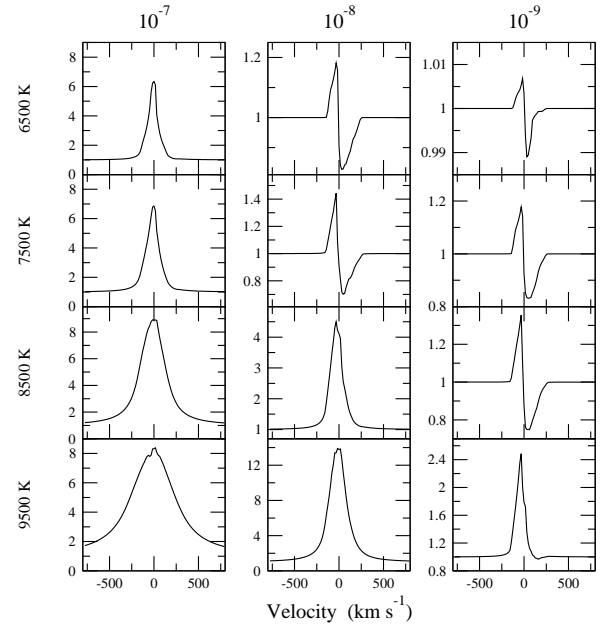


Figure 5. H α model profiles for wide ranges of mass accretion rate (\dot{M}_{acc}) and temperature (T_{\max}). The profiles are computed using only magnetospheric accretion flow (i.e. no wind/jet). All the profiles are computed using the parameters of the ‘‘standard’’ model (Table 1) and inclination $i = 55^{\circ}$. The temperature (indicated along the vertical axis) of the model increase from top to bottom, and the mass accretion rate (indicated by the values in $M_{\odot} \text{ yr}^{-1}$ at the top) increases from left to right. The profiles are similar to those of Muzerolle et al. (2001), available on-line (http://cfa-www.harvard.edu/cfa/youngstars/models/magnetospheric_models.html).

the density in polar direction to the density at the edge of the wind closest to the accretion disc is about $(\cos 0^{\circ} / \cos 80^{\circ})^4 \approx 10^3$, for given radii. For simplicity, the wind temperature T_{wind} is assumed to be isothermal. Although the line is potentially sensitive to the temperature structure of the wind, determination of a self-consistent wind temperature is beyond the scope of this paper. Readers are referred to Hartmann et al. (1982) in which the wind temperature structure is determined by balancing the radiative cooling rate (assuming optically thin) with the MHD wave heating rate. With these parameters kept constant, we examine the characteristics of H α profiles, as a function of the wind acceleration parameter β and the isothermal wind temperature T_{wind} . Dependency on the other parameters will be discussed later in this section.

Figure 8 shows the profile computed at a mid inclination angle $i = 55^{\circ}$ for the range of the wind temperature between 7000 K and 9000 K, and for the range of β between 0.2 and 2.0. The P Cygni profiles are prominent in the models with lower values of T_{wind} and β (colder and faster acceleration wind). As the value of β increases, the position of the blue-shifted absorption component moves toward the line centre, which can be seen clearly in the $T_{\text{wind}} = 7000 \text{ K}$ models. While the velocity position of absorption component for the fastest acceleration ($\beta = 0.2$) is almost at the terminal velocity ($v_{\infty} \sim 210 \text{ km s}^{-1}$), that for the slowest wind acceleration model ($\beta = 4.0$) is located close the line centre ($\sim 50 \text{ km s}^{-1}$). As one can see in Figure 2, the column density of the gas moving at v_{∞} increases as the wind acceleration becomes larger since the gas moving at v_{∞} becomes closer to the photosphere. At the location where the absorption occurs, the gas is moving faster for the models with the faster wind acceleration mod-

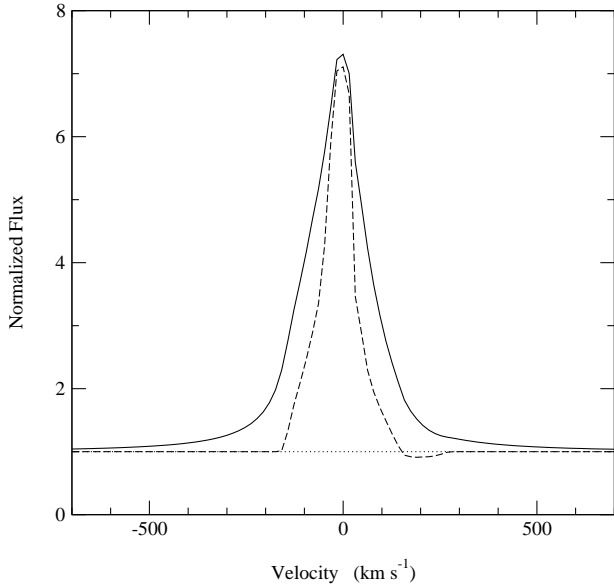


Figure 6. The effect of line broadening for $H\alpha$. The model computed with a damping constant (Γ), described in section 3 (solid), is compared with the model with no damping, $\Gamma = 0$ (dashed). Both models are computed with $T_{\max} = 7500$ K, $i = 55^\circ$, and the standard parameters given in Table 1. The two models have similar peak flux levels (around $V \sim 0$ km s^{-1}), but the total flux and the EW of the line increased drastically for the model with the damping constant. The broad wings extend to $\sim \pm 800$ km s^{-1} . The redshifted absorption feature (very weakly) seen in the $\Gamma = 0$ model is not seen in the model with the broadening.

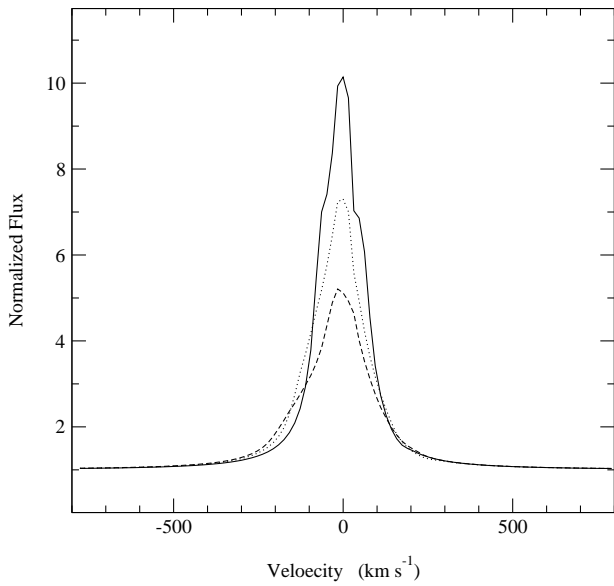


Figure 7. Dependency of $H\alpha$ profiles on inclination (i). The profiles are computed with the magnetospheric accretion flow using the standard parameters given in Table 1 and $T_{\max} = 7500$ K. The solid, dotted, and dashed lines are for $i = 10^\circ, 55^\circ$, and 80° respectively. As the inclination becomes larger, the peak flux and the equivalent width of the line becomes smaller. Similar dependency is seen in the models with the wide ranges of T_{\max} and β .

els; hence, the location of the absorption component is bluer as β becomes smaller (as the wind acceleration faster). The figure also shows that the intensity of the emission component increases as β increases for a given T_{wind} . This is mainly because the density near the photosphere increases as the value of β increases (Figure 2); hence, the emissivity of increases. Unlike the magnetospheric accretion only models (Figure 5), the inverse P Cygni profiles are not seen here, nor the blue-ward asymmetry. Because of the absorption component in P Cygni profile, most of the profiles show red-ward asymmetry except for the low temperature wind models with high inclinations (not shown here).

The dependency of the profile on the wind anisotropy parameter b is demonstrated in Figure 9. Three models presented in the figure have the same mass-loss rate ($10^{-8} M_{\odot} \text{ yr}^{-1}$), and are computed at inclination angle $i = 55^\circ$. The P Cygni profile feature becomes more prominent, and the line flux becomes smaller as the wind becomes more isotropic (smaller b value). For a fixed mass-loss rate, the column density of along the line of a sight to the observer at a medium inclination angle (e.g. $i = 55^\circ$) increases as b decreases (c.f. equation 8); hence, causing more absorption. Furthermore, the value of the highest density in the wind becomes smaller for a smaller b model. As the wind becomes more isotropic, the material in the polar direction has to be spread in the wider angular angles. This results in a smaller highest density region in the wind; hence the smaller line emissivity. For the same reason, the emission in the wings is weaker for the model smaller b value. We also note that the asymmetry around the line centre decreases as the wind becomes more isotropic.

The effect of varying the wind mass-loss rate is shown in Figure 10. The line is very sensitive to the mass-loss rate. With all other parameters fixed constant, \dot{M}_{wind} acts as a scaling factor of the wind density (equation 8). The important processes in forming $H\alpha$ emission are the recombination process and the subsequent downward transition to $n = 3$ level. Assuming the ionisation fraction remains constant, the recombination rate is proportional to the square of wind density. We have found the line flux of the models in the figure is approximately proportional to the square of the mass-loss rate. This very sensitive nature of $H\alpha$ would make the line a good candidate for a mass-loss rate indicator; however, without solving the ambiguity of the emission component from the magnetospheric accretion flow and the wind, and without knowing the detailed temperature structure of the wind, it could provide us a misleading a mass-loss rate estimate of a T Tauri star.

4.3 Disc +bipolar wind

Next, we examine the effect of the size of the inner radius of the disc and the distribution of the $H\alpha$ emission region. Figure 11 shows the wind emission profiles computed with and without the accretion disc at $i = 55^\circ$. The $H\alpha$ images (projected on to the plane perpendicular to the observer at the location of the star) are also shown in the same figure. Both models use the same parameters as in Figure 8, but with $\beta = 0.5$ and $T_{\text{wind}} = 9000$ K. The model without the disc can be also considered as a model with a large inner radius of the accretion disc, in which none of the wind emission region is blocked by the disc — provided the inclination angle is not high and the disc is not or slightly flared.

The bipolar nature of the wind is clearly seen in the images. In this example, the most of the wind emission occurs within a few to a several (depending mainly on the value of β) stellar radii from the star. The figure also shows that the accretion disc blocking the wind emission from the bottom half of the wind which is moving

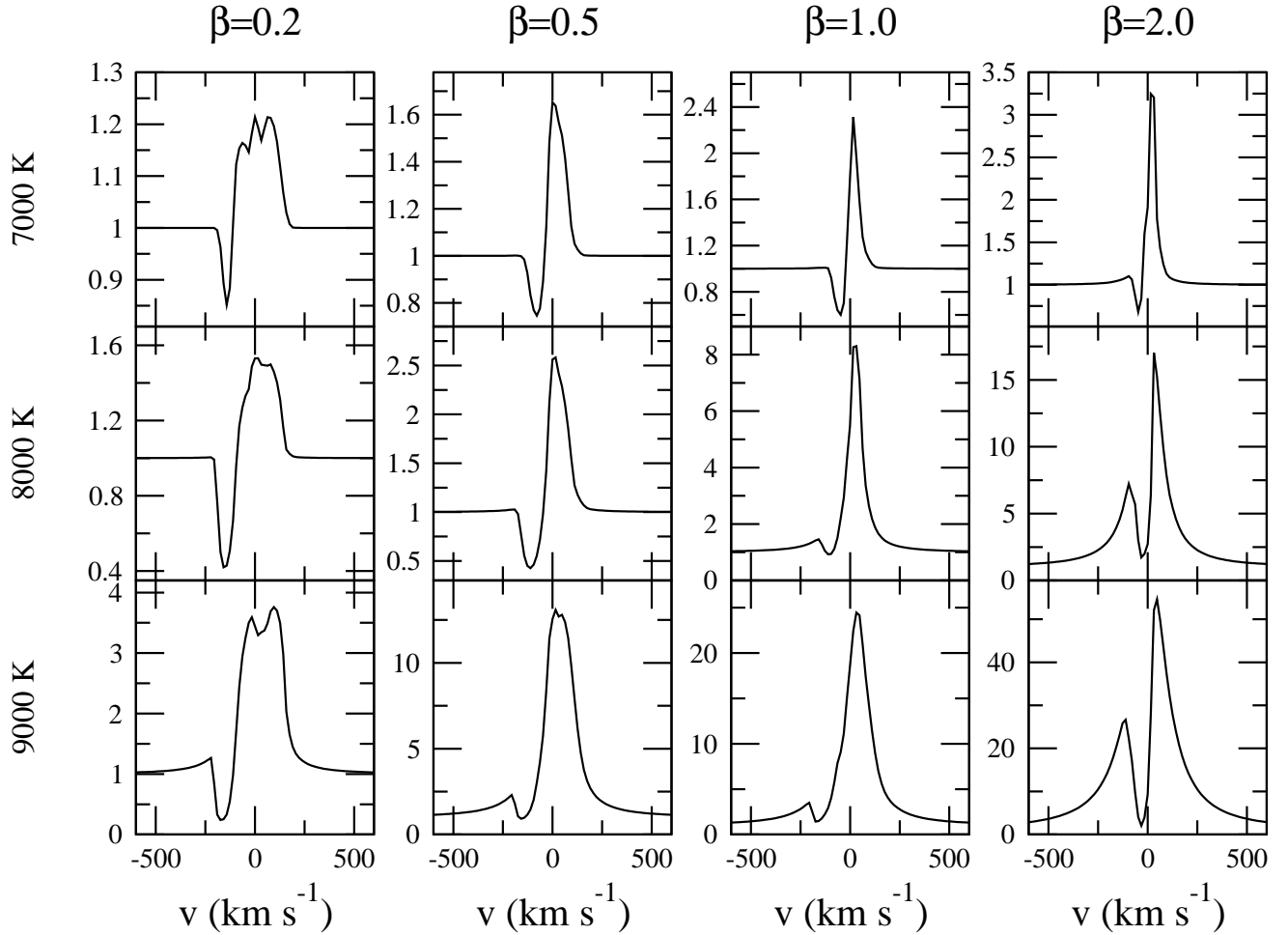


Figure 8. H α model profiles computed with wide ranges of the isothermal wind temperature (T_{wind}) and the wind acceleration rate (β). The profiles are computed with the wind component only (no magnetospheric accretion flow or accretion disc). The ‘standard’ model parameters (Table 1) are applied. The wind mass-loss rate (\dot{M}_{wind}), the inclination (i) and the degree of columniation (b) are fixed at $10^{-8} M_{\odot} \text{ yr}^{-1}$, 55° and 4.0 respectively. The temperature (indicated along the vertical axis) of the model increases from top to bottom, and the wind acceleration rate increases from left to right. The P Cygni profile are seen for lower T_{wind} and lower β (slow acceleration) models. The position of the absorption the component moves toward the line centre as β increases. The effect of line broadening becomes more prominent for higher T_{wind} and higher β models.

away from the observer. This results in the reduction of the wind emission in the red wing. The image (mid panel) also shows that the accretion disc is not occulting the stellar disc at this inclination; therefore, the ratio of the wind emission flux to the photospherical continuum flux becomes slightly smaller for the model with the disc. This results in the reduction in the peak flux and the flux in the wings in the normalised profile shape. If the disc becomes more flared (if the opening angle exceeds 45° at the outer edge of the accretion disc), the occultation of the stellar disc by the accretion could be seen at this inclination angle. Although it is not shown here, the continuum level of the two models are identical. For the models with $i < 30^\circ$, the presence of the disc has little/no effect on the profile shapes. In the figures, the extent of the H α emission is smaller (~ 0.2 au or $\sim 20 R_*$) compared to the spectro-astrometric observations of Takami et al. (2003) for RU Lup and CS Cha which show 1–5 au scale outflows¹; however, the extent of the line emis-

sion region becomes slightly larger (~ 0.4 au) if a slower wind acceleration rate ($\beta = 4$) is used.

Although not shown here, we have also computed the H α profiles from the combination of the collimated wind and the accretion disc ($R_{\text{di}} = 2.2 R_*$ and $R_{\text{do}} = 100$ au) for the same range of β and T_{max} values used in Figure 8. As expected (c.f. Figure 11), the models show the decrease in the flux in the blue wing when compared to the flux of the same model computed without the accretion disc. The overall behaviour of the line profile shapes as functions of β and T_{wind} are very similar to that for the models without the accretion disc. A significant reduction of the flux in the red wing is seen in the wind model with the accretion disc when compared with the wind only model. The wings appear to be weaker in these models compared to the wind only models because the ratio of the wind emission flux to the continuum flux is lower.

¹ Takami et al. (2003) their observation also show that some objects (e.g Z CMa and AS 353A) displaying the outflows of larger scale (> 50 au); how-

ever, this could be formed by shocks rather than MHD-wave heating (e.g. Hartmann et al. 1982) or X-ray heating (e.g. Shang et al. 2002).

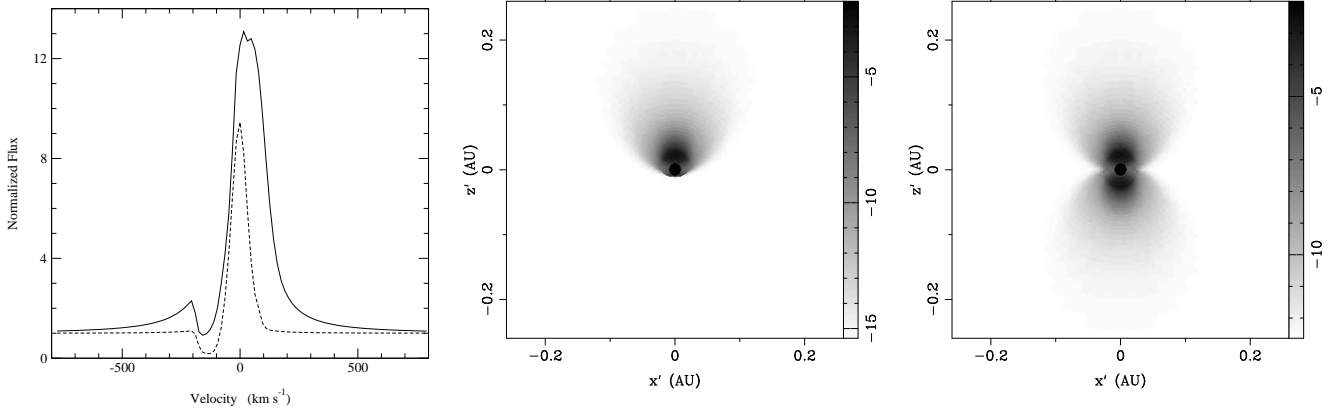


Figure 11. A comparison of the wind models with and without the optically-thick and geometrically-thin disc. The latter can be also equivalent to a model with a large inner radius of the accretion disc in which none of the wind emission region is not blocked provided the inclination is moderate. The left panel shows the profile computed with $i = 55^\circ$, $\beta = 0.5$ and $T_{\text{wind}} = 9000$ K (see text for other parameters used). The flux in the red wing of the line profile from the model with the disc (solid) is greatly reduced by the presence of the accretion disc compared to that from the model without the disc (dashed). The peak flux and the flux in the wings are also reduced in the model with the disc because the disc blocks the wind emission region, but none of the stellar disc, i.e. the continuum flux level is unchanged. The H α image (project in the plane of the observer) for the model with the disc (middle panel) and that for the model without (right plane) are also shown. The image flux is computed by integrating the specific flux over the wavelength range $-800 \text{ km s}^{-1} < v < 800 \text{ km s}^{-1}$. The flux is in an arbitrary units and on a logarithmic (base 10) scale.

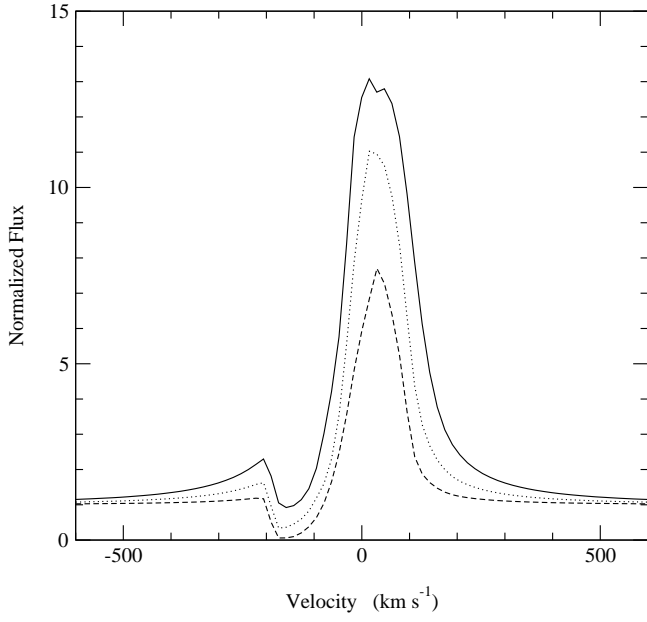


Figure 9. The effect of wind collimation. The line profiles computed with with $(T_{\text{wind}}, \beta) = (9000\text{K}, 0.5)$ for the wind anisotropy parameter $b = 0, 2, 4$ are shown in dashed, dotted, and solid respectively. All the other parameters are same as in Figure 8. The P Cygni profile feature becomes prominent for the spherical wind model since the column density of along the line of a sight of the observer at a mid inclination angle ($i = 55^\circ$) increases for lower b values for a fixed mass-loss rate of the wind. The blueward asymmetry is still present even in the isotropic wind case ($b = 0$).

4.4 Magnetosphere + disc +bipolar wind

We examine the characteristics of the line profiles arising from the combination of the magnetospheric accretion flow, the wind, and the accretion disc. For simplicity, the parameters for the magnetosphere ($T_{\text{max}} = 7500$ K and $M_{\text{acc}} = 10^{-7} \text{ M}_\odot \text{ yr}^{-1}$ are

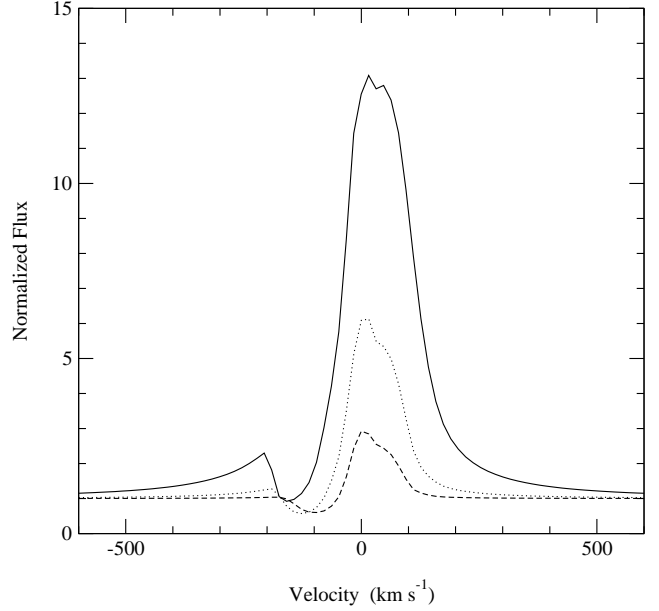


Figure 10. The effect of the wind mass-loss rate. The profiles computed with $(T_{\text{wind}}, \beta) = (9000\text{K}, 0.5)$, and $\dot{M}_{\text{wind}} = 1.0 \times 10^{-8} \text{ M}_\odot \text{ yr}^{-1}$ (solid), $0.5 \times 10^{-8} \text{ M}_\odot \text{ yr}^{-1}$ (dotted), and $0.25 \times 10^{-8} \text{ M}_\odot \text{ yr}^{-1}$ (dashed) are shown above. The models are computed with only the wind component (no magnetospheric accretion flow or accretion disc). With all other parameter fixed constant, the mass-loss rate behaves as a scaling factor for the wind density (equation 8).

fixed as in Figure 5), and the wind mass-loss rate, the isothermal wind temperature and the wind anisotropy parameter to $\dot{M}_{\text{wind}} = 10^{-8} \text{ M}_\odot \text{ yr}^{-1}$ (i.e. $\dot{M}_{\text{wind}} = 0.1 \dot{M}_{\text{acc}}$), T_{wind} and $b = 4$ respectively. The profile computed for $i = 55^\circ$ is given in Figure 12, along with the profile computed with the magnetosphere only and that with the wind plus accretion disc configurations for a comparison. As one can see from the figure, the profile computed for

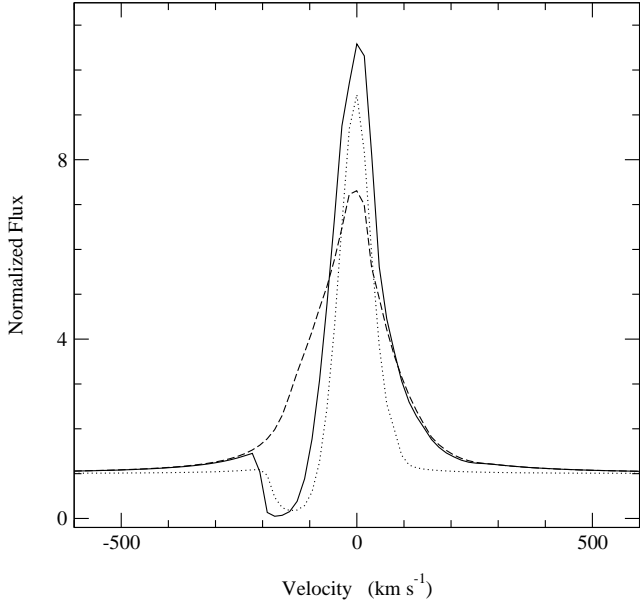


Figure 12. A comparison of the profiles computed with the magnetosphere, the wind, the disc, and their combinations. The model configurations used above are: (1) magnetosphere only (dash), (2) wind and disc (dot), and (3) disc, wind and magnetosphere (solid). The parameters used here are $T_{\max} = 7500$ K, $\dot{M}_{\text{acc}} = 10^{-7} M_{\odot} \text{ yr}^{-1}$, $\dot{M}_{\text{wind}} = 10^{-8} M_{\odot} \text{ yr}^{-1}$, $T_{\text{wind}} = 8000$ K, and $\beta = 0.5$. The profile for the case 3 is can be understood as a simple flux sum of the profiles from case 1 and 2.

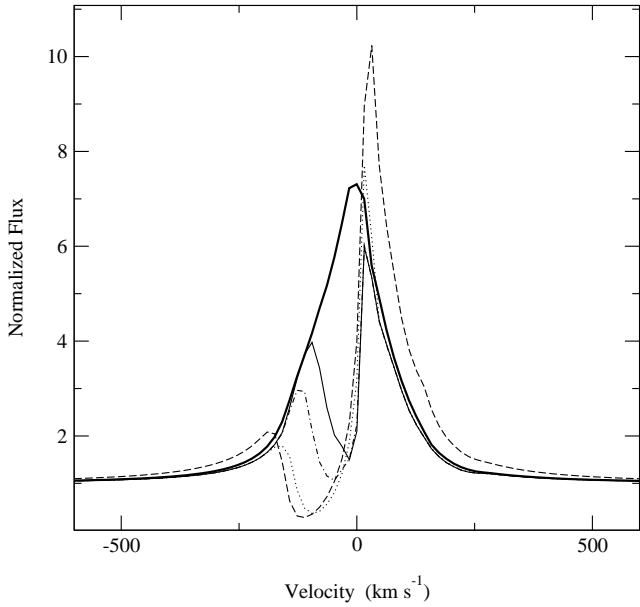


Figure 13. The effect of the mass-loss rate to mass-accretion rate ratio ($\mu = \dot{M}_{\text{wind}}/\dot{M}_{\text{acc}}$). The $\text{H}\alpha$ profile computed with only the magnetospheric accretion (thick solid) — $T_{\max} = 7500$ K, $\dot{M}_{\text{acc}} = 10^{-7} M_{\odot} \text{ yr}^{-1}$ — is compared with the magnetosphere, wind, and disc hybrid models for $\mu = 0.01$ (solid), 0.025 (dash-dot), 0.1 (dot) and 0.2 (dash). All the models are computed with the inclination angle $i = 55^\circ$. As μ increases the P-Cygni absorption deepens and the emission component becomes stronger. In general, the absorption is too strong for the models with $\mu > 0.025$ compared to the observations (e.g., Reipurth et al. 1996).

the disc–wind–magnetosphere hybrid model can be understood as a simple flux sum of the magnetospheric component and the wind component. In this example, the wind causes the absorption of the blue side of the profile, and it adds extra flux around the line centre. As seen before, the presence of the disc causes a reduction in the red side of the profile since the emission from the receding gas is blocked by the disc. The resulting profile appears to be narrower than that of the magnetosphere model.

The effect of changing the ratio of the wind mass-loss rate to mass-accretion rate ($\mu = \dot{M}_{\text{wind}}/\dot{M}_{\text{acc}}$) is demonstrated in Figure 13. With a fixed value of mass-accretion rate ($\dot{M}_{\text{acc}} = 10^{-7} M_{\odot} \text{ yr}^{-1}$), the mass-loss rate is varied. The figure shows that as μ increases the P-Cygni absorption deepens, and the position of minimum flux in the absorption trough appears to move blue-ward. On the other hand, the emission component becomes stronger as μ increases. With this combination of the parameters for the magnetosphere and the wind, the absorption component tends to be too strong for the models $\mu > 0.025$ (with this model configuration), at all inclinations (not shown here), compared with the observed $\text{H}\alpha$ profiles (e.g. Reipurth et al. 1996; Alencar & Basri 2000).

Again, the $\text{H}\alpha$ profiles with the same range of the wind temperature (T_{wind}) and the wind acceleration parameter (β) used in Figure 8 are computed, but this time with $\mu = 0.01$. The parameters of the magnetosphere are fixed as in Figure 7. The results are shown in Figure 14 along with the model with only the magnetosphere for a comparison. A relatively small value of μ is chosen to avoid absorption component of the P-Cygn profile becoming too strong, as seen in Figure 13. In general, even with small values of the anisotropy parameter ($b = 0$ and 2), the absorption component is found to be too strong when $\mu = 0.1$ is used with this combination of the magnetosphere and the wind. The figure shows that the position of the wind absorption component moves toward the line centre as β becomes larger. Although little wind emission is seen in this temperature range, it becomes more important in a model with a higher temperature and a larger wind mass-loss rate. In fact, the model with $\beta = 2.0$ and $T_{\text{wind}} = 9000$ K displays a small amount of the wind emission at $V \sim 50 \text{ km s}^{-1}$.

As seen in Figure 12, the profiles shown here can be understood as the combination of the emission from the magnetosphere and the absorption of the flux by the wind component. In general, the emission from the accretion disc is negligible at $\text{H}\alpha$ wavelength, but the absorption of the continuum flux from the photosphere by the disc is important for predicting correct line strengths, especially at a high inclination.

Although the profiles shown in Figure 14 are those at a single inclination angle ($i = 55^\circ$), they are very similar to the most common types of $\text{H}\alpha$ profiles seen in the observations (e.g. Reipurth et al. 1996). Apparently, this type of profile (affected by the blue-shifted absorption feature) cannot be explained by the magnetospheric accretion flow alone (e.g. Muzerolle et al. 2001). Comparison of the model profiles with different types of the observed $\text{H}\alpha$ profiles will be given in section 5.1.

4.5 Disc-wind model of Knigge et al. (1995)

As an alternative model for the bipolar wind models (with the combination of the magnetosphere and the accretion disc) shown in Figures 8 and 14, we have also considered the disc-wind model of Knigge et al. (1995) as described in section 4.3. The former resembles the density structure of Krasnopol'sky et al. 2003 in large scale (~ 100 au) which described in section 2.3.1, and the latter in small scale (~ 10 au) of the same model. The main difference between

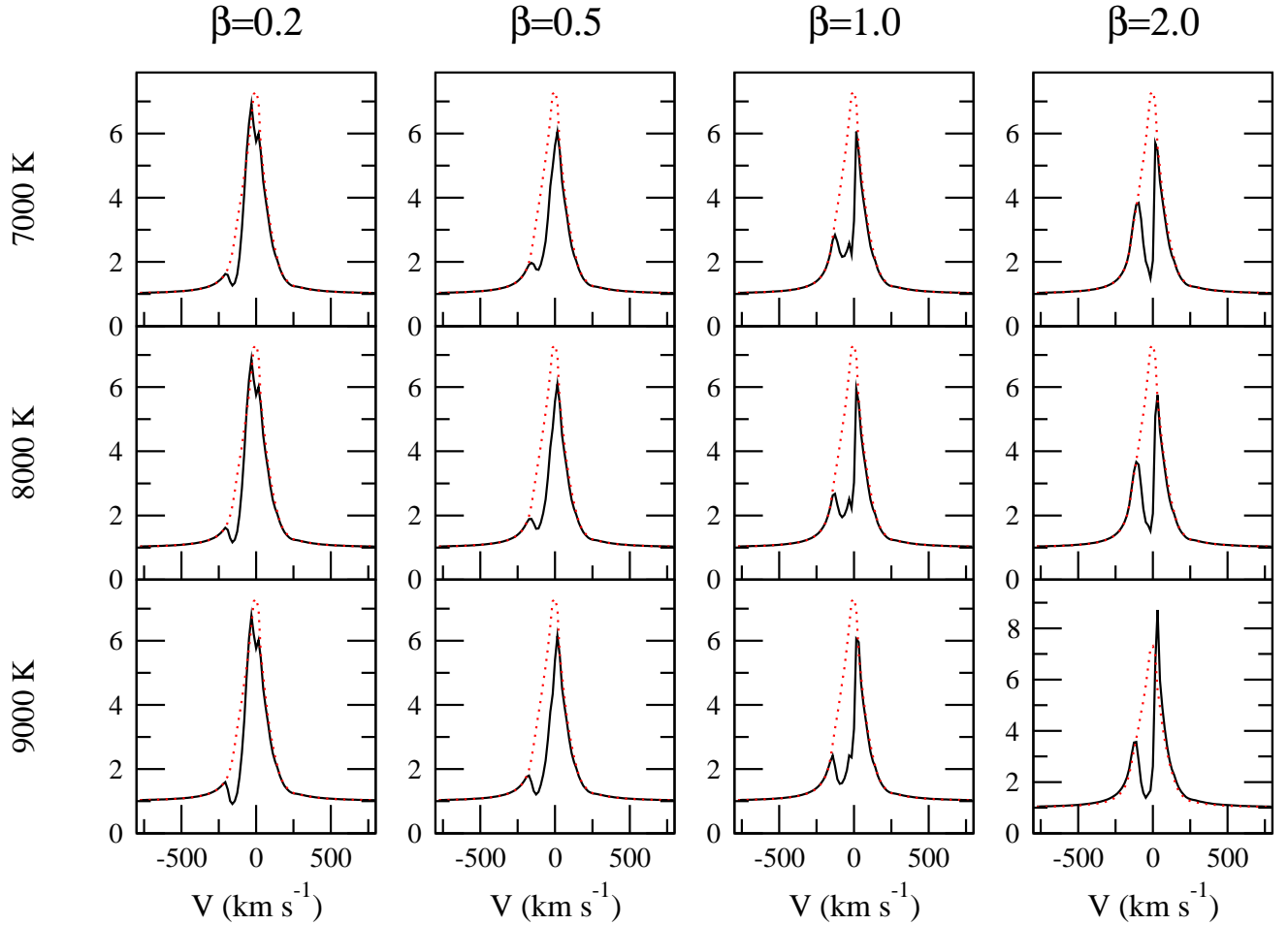


Figure 14. Same as Figure 8, but the models include the magnetospheric accretion flow (with $T_{\max} = 7500$ K and $\dot{M}_{\text{acc}} = 10^{-7} M_{\odot} \text{ yr}^{-1}$), and the accretion disc. The mass-loss rate of the wind is $\dot{M}_{\text{wind}} = 10^{-9} M_{\odot} \text{ yr}^{-1}$. A relatively small mass-loss rate is chosen to avoid unrealistically strong P-Cyg absorption component (see text in section 4.4 and Figure 13). For a comparison, the profile computed with only the magnetospheric accretion flow (dotted) is overlayed. All the profiles are computed at the inclination angle $i = 55^\circ$. As β becomes larger, the position of the wind absorption component moves toward the line centre. Although little wind emission is seen in this temperature range, it becomes more important in a model with a higher temperature and a larger wind mass-loss rate. The profiles resemble the observed H α emission profiles affected by the wind.

the two models are in their density structure. At a given radius, the density increases toward the polar direction in the former model, but the density increases toward the equatorial plane for the models presented here.

First, the disc-wind models without the magnetosphere are considered. Figure 15 shows the H α profiles computed using only the disc-wind component (c.f. Figure 3) for the same isothermal disc-wind temperature (T_{dw}) and the wind acceleration parameter (β) ranges used for the bipolar wind models. The parameters used for the central star are as in section 2.1, and the other disc-wind parameters are summarised in Table 3. The figure shows that the wind emission increases as β and T_{dw} increase. Similar to the bipolar wind models, the location of the P-Cyg absorption component moves toward the line centre as β increases. The morphology of the profile exhibited by the model changes from FU-Ori type for the models with small β to the stronger emission types which are more commonly seen in the observed H α (c.f. Reipurth et al. 1996) as the value of β increases. Although not shown here, we find that the profile shapes are relatively insensitive to the value of the wind collimation parameter d . The dependency on the disc wind mass-

loss rate of the profile shape is similar to that of the collimated wind models (Figure 13).

We now consider the models computed with the combination of the disc-wind and the magnetospheric accretion components. The parameters used for the magnetosphere are set to be same as in the case for Figure 7, and are kept constant for simplicity. The mass-loss rate of the disc wind is set to $\dot{M}_{\text{dw}} = 10^{-8} M_{\odot} \text{ yr}^{-1}$ (i.e. $\mu = \dot{M}_{\text{dw}}/\dot{M}_{\text{acc}} = 0.1$). Figure 16 shows the models profiles computed using the same ranges of the disc-wind temperature and the wind acceleration parameter as in the previous cases.

As in the disc wind only models (Figure 15), the location of the absorption component moves toward the line centre as the value of β increases (the wind acceleration is slower). The figure shows that in the models with smaller β and T_{dw} , the line emission from the magnetosphere dominates. On the other hand, in the models with larger β and T_{dw} , the emission from the disc wind dominates. Compared to the observation of Reipurth et al. (1996) and Alencar & Basri (2000), the lines are too strong for $(T_{\text{dw}}, \beta) = (9000 \text{ K}, 2.0)$ and $(9000 \text{ K}, 1.0)$ models.

Although the models in Figure 16 are computed with limited

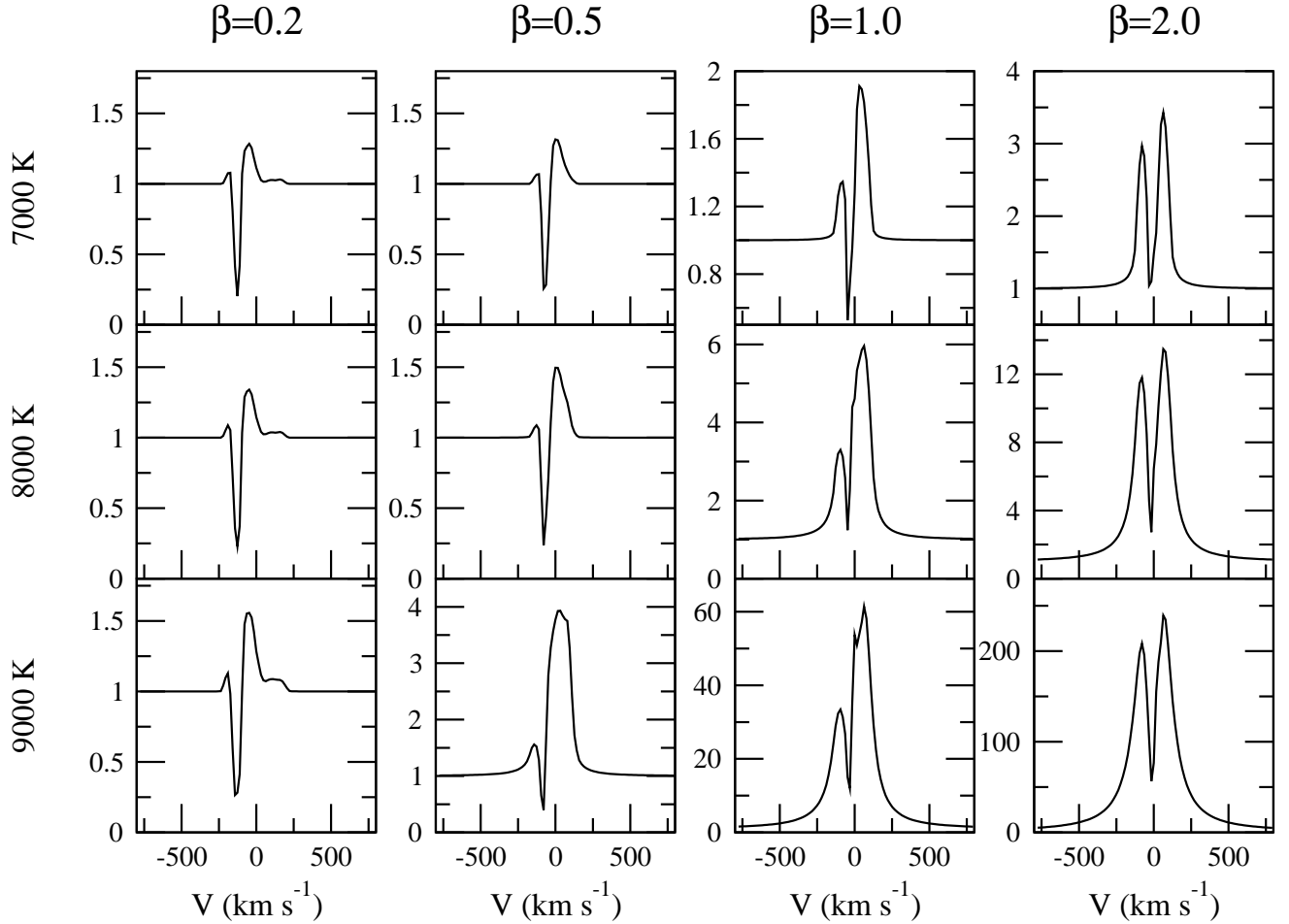


Figure 15. The H α profiles computed with the disc-wind only models. With the wind mass-loss rate fixed at $\dot{M}_{\text{dw}} = 10^{-8} M_{\odot} \text{ yr}^{-1}$, the line profiles are computed with different combinations of the wind acceleration rate (β) and the isothermal disc-wind temperature (T_{dw}). The wind emission increases as the values of β and T_{wind} increase (as the wind becomes accelerates slower and as the wind comes warmer. As in the bipolar wind models (Figure 8), the position of the wind absorption moves toward the line centre as β becomes larger. The morphology of the profiles are similar to that of observations.

ranges of T_{dw} and β , the resulting profiles exhibit the wide varieties of line shapes which are very similar to the types of H α profiles seen in the observations (c.f. Reipurth et al. 1996). The shape of the primary and secondary peaks in the profiles are slightly “rounder” compared to those of the accretion, collimated wind, disc hybrid model shown in Figure 14. The rounder peaks are caused by the rotation of the wind. The profiles from the disc-wind models are affected more by the rotational motion of the wind since the gas is more concentrated toward the equator, but in the models with the collimated wind the gas is concentrated more in the polar directions.

We note the ambiguity seen between some of the disc-wind only models and the disc-wind, magnetosphere hybrid models. For example, the disc-wind only model with $(T_{\text{wind}}, \beta) = (8000 \text{ K}, 1.0)$ in Figure 15 and the disc-wind model with $(T_{\text{wind}}, \beta) = (9000 \text{ K}, 0.5)$ in Figure 16 give very similar profiles. Given such an observed profile, it is difficult to distinguish if the emission is dominated by the accretion or the wind unless some other lines, not affected associated with wind or magnetosphere, are used simultaneously.

General characteristics of the profiles from the disc-wind, magnetosphere hybrid model (Figure 16) are very similar to those

Table 3. A summary of the standard disc-wind model parameters used in section 4.5. See also section 2.3.2.

d [R_{\ast}]	R_{wi} [R_{\ast}]	R_{wo} [au]	\dot{M}_{dw} [$M_{\odot} \text{ yr}^{-1}$]	p [-]	f [-]	R_s [R_{\ast}]
21.4	3.0	1.0	10^{-8}	-3/2	2.0	30

of the disc, collimated wind, magnetosphere hybrid model (Figure 14). The main difference between these two sets of models is in the ration of the mass-loss rate to the mass accretion rate, μ . While the models presented in this section use $\mu = 0.1$ which is consistent with the MHD jet models (e.g. Königl & Pudritz 2000), the models in Figure 14 use much smaller value ($\mu = 0.01$). The dependency of the model profiles on the inclination angle for the two different wind models will be discussed in the next section.

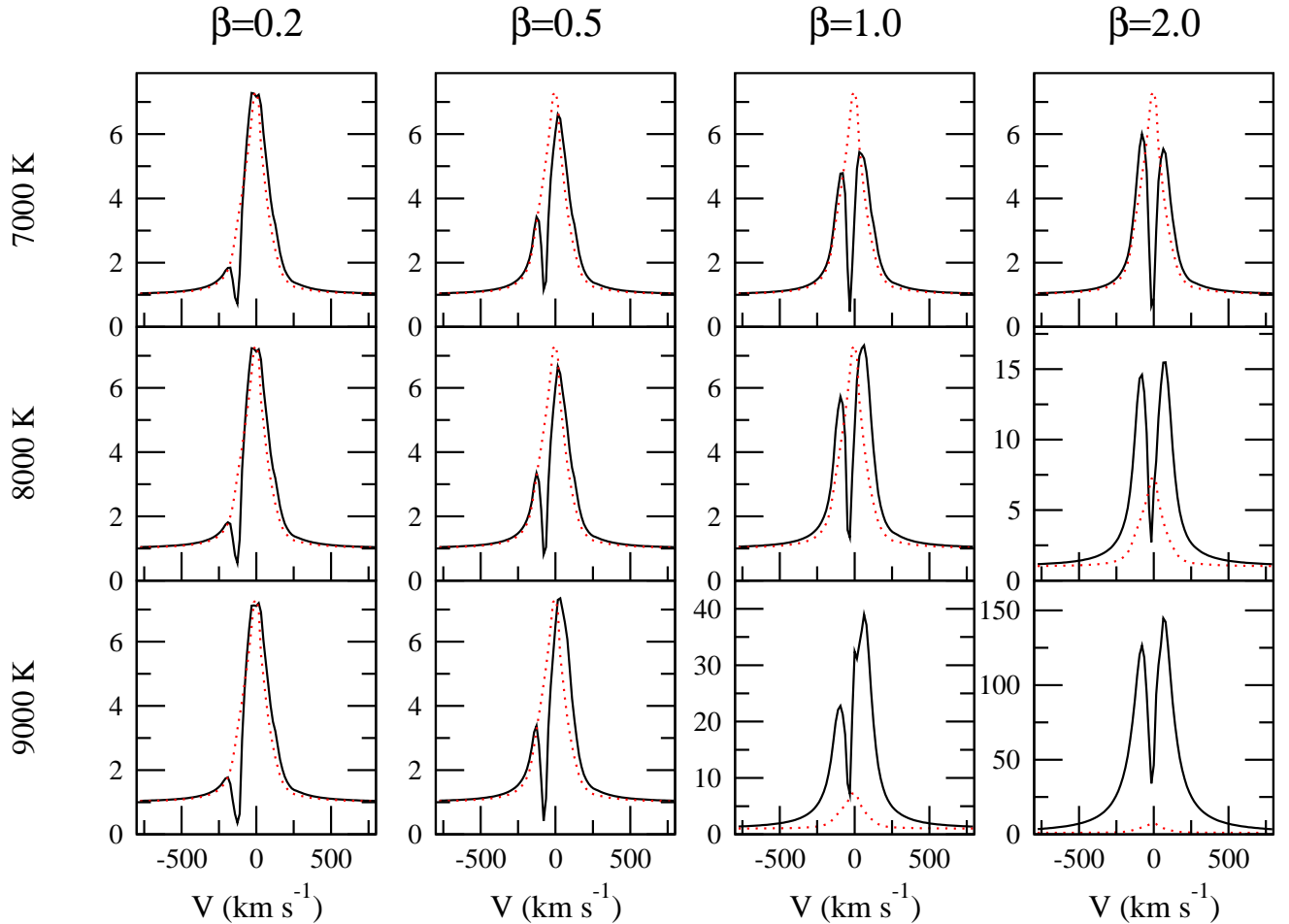


Figure 16. The disc-wind, magnetosphere hybrid model. The same as Figure 15, but these models (solid) also include the magnetosphere accretion flow ($T_{\max} = 7500$ K and $\dot{M}_{\text{acc}} = 10^{-8} M_{\odot} \text{ yr}^{-1}$). While the emission from the magnetosphere dominates for the models with smaller β and T_{dw} (the faster acceleration and the colder wind models), the emission from the wind dominates the profiles for models with larger β and T_{dw} (the slower acceleration and the hotter models). For a comparison, the profile computed with only the magnetospheric accretion flow (dotted) is overlayed.

5 DISCUSSION

5.1 Classification scheme proposed by Reipurth et. al (1996)

Reipurth et al. (1996) proposed the two-dimensional classification of $H\alpha$ emission profiles of T Tauri stars and Herbig Ae/Be stars. Their classification scheme contains four classes (I, II, III and IV) differentiated by the ratio of the secondary-to-primary emission components in the profiles. Each classes are divided into two subclasses (B and R) which depends whether the absorption component is on the blue or red side. Readers are referred to Fig. 4 of their paper. Figure 17 shows the sample model profiles which are classified according to the definition of Reipurth et al. (1996). The combination of the disc wind, magnetospheric accretion, and accretion disc can reasonably reproduce all the classes of the profiles seen in observations. Similar profiles can be reproduced if the bipolar wind is used instead of the disc wind, but the wind absorption at a given velocity location occurs at a different inclination angles when the wind type is switched from the bipolar wind to the disc wind. The corresponding parameters (of the disc-wind, magnetosphere, hybrid model) used to reproduce the profiles in the figure are given in Table 4 along with brief comments on possible physical conditions which leads to the profiles in each class. In the fol-

lowing, we will discuss each classification type of Reipurth et al. (1996) based on our model results.

Type I: Using the samples of $H\alpha$ from 43 CTTS, Reipurth et al. (1996) found this type to be the second most common (26 per cent) among them. Type I (symmetric around line centres), is mainly produced in the magnetosphere. Although not shown here, this type of profile can be also reproduced with the disc-wind, magnetosphere hybrid model with low inclination angles ($<\sim 10^\circ$). Since there is no material in the polar region in the disc wind model, the observer can look the magnetosphere almost directly for high inclination cases, provided that wind temperature is low enough so that the wind emission is negligible. The bipolar wind, magnetosphere and accretion hybrid model with high inclination ($70^\circ - 80^\circ$) can also give this type of profile since the influence of the bipolar wind is minimum in the equatorial directions. The wind acceleration parameter for the bipolar wind must be relatively small ($\beta <\sim 0.5$).

Type II-B: This type can be produced by the disc-wind magnetosphere hybrid models at moderate to high inclination angles with wide ranges of the wind acceleration rate ($\sim 0.2 < \beta <\sim 2.0$) and the wind temperature ($\sim 7000 \text{ K} < T <\sim 9000 \text{ K}$). If the inclination is high ($i \sim 80^\circ$), the disc-wind acceleration pa-

rameter should be relatively small ($\beta < \sim 0.5$). If the inclination is moderate ($i \sim 60^\circ$), the wind acceleration parameter should be relatively high ($\beta > \sim 2.0$). This type can be also produced in the bipolar wind, magnetosphere disc hybrid model with similar ranges of inclinations ($\sim 60^\circ < i < \sim 80^\circ$) and temperatures ($\sim 7000 \text{ K} < T < \sim 9000 \text{ K}$), but the wind acceleration should be always high ($\beta > \sim 1.0$).

Type II-R: The physical conditions which result in this type is very similar to those of Type II-B according to the disc-wind magnetosphere hybrid models. The main difference is between the two is in their inclination angles. This type is more likely seen at higher inclination angles ($i \sim 80^\circ$) compared to Type II-B. With the bipolar wind model, the wind acceleration parameter must be very large ($\beta \sim 6.0$) to produce this type, and the inclination must be moderate to low ($i < \sim 60^\circ$). This type is rarely seen in the bipolar wind models with the nominal parameter ranges i.e. $\sim 0.2 < \beta < \sim 2.0$ and $\sim 7000 \text{ K} < T < \sim 9000 \text{ K}$. More common in the models with the disc wind.

Type III-B: This type is the most commonly seen profiles in the CTTS H α samples in Reipurth et al. (1996). Interestingly, the most common profile type seen in both the bipolar wind, disc, magnetosphere hybrid models and the disc-wind, magnetosphere hybrid model are Type III-B profiles (c.f. Figures 14 and 16). In this type of profiles, the main emission comes from the magnetosphere, and the profile shape is altered from a slightly blue-asymmetric one to a slightly red-asymmetric one via the wind absorption in the blue wing. In the models with the disc-wind, the acceleration parameter should be relatively small ($\beta < 0.5$). The profile type changes from Type III-R to Type II-R if the value of β increases. The inclination angles must be moderate to high ($\sim 60^\circ < i < \sim 80^\circ$). On the other hand, the inclination must be low to moderate ($i < \sim 60^\circ$) in the models with the bipolar wind. The difference in the inclination dependency occurs since the density distribution of the two types of the winds are different.

Type III-R: This is the least common type of the observed profile (2 per cent) according to Reipurth et al. (1996). Incidentally, we also found it difficult to reproduce this type of profile since this can be achieve only at narrow range of parameter space (very high inclination angle with a disc wind model, $T_{\max} \sim 8300 \text{ K}$, and $\dot{M}_{\text{acc}} \sim 10^{-8} \text{ M}_\odot \text{ yr}^{-1}$). Similarly, in the models with the bipolar wind, the inclination angle must be very high (close to edge on) to produce this type of profile. Since the inclination angles must be high for both wind models, this indicates that the accretion disc plays an important role in producing this type of the profile, but not the wind. The rareness of this type in the observation can be understood by the required high inclination angle (almost edge-on) in our models.

Type IV-B: This type of the profiles is very similar to Type III-B, but the wind in this type of profile may be accelerating faster (a smaller β value) than that in Type III-B. In the models with the disc-wind, this type is seen at moderate to high inclinations ($\sim 60^\circ < i < \sim 80^\circ$) with relatively small value of the acceleration parameters ($\beta < \sim 0.5$). In the models with the bipolar wind, this type is commonly seen at moderate to low inclinations ($i < \sim 60^\circ$). The difference in the inclination dependency occurs because of the density distribution of the two types of the winds are different.

Type IV-R: This is the second least common type of observed profile (5 per cent) which shows the inverse P-Cyg profile shape. This can be understood since the magnetospheric accretion model of Hartmann et al. (1994) predicts that the redshifted absorption can occur at a limited range of inclination angle ($i = \sim 50^\circ$,

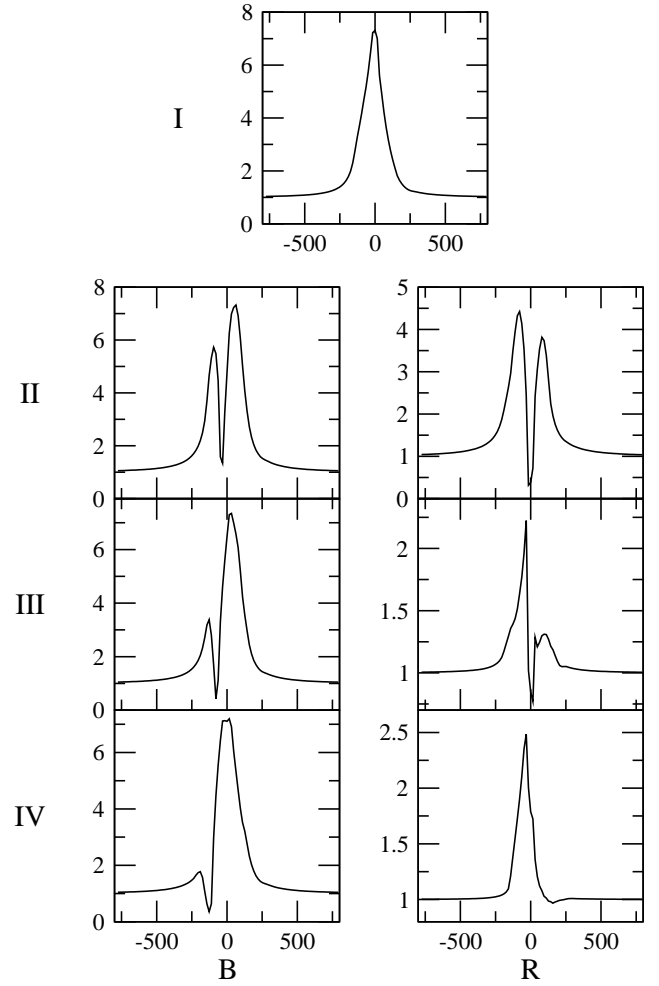


Figure 17. Sample H α model profiles which characterise the classification by Reipurth et al. (1996). The combination of magnetospheric accretion flow, the accretion disc, and the disc wind model can reasonably reproduce wide ranges of H α profiles seen in observations. Similar results can be obtained if the bipolar wind is replaced by the disc wind. The model parameters and short comments are summarised in Table 4. The horizontal axes are velocities in km s^{-1} , and the vertical axes are normalised flux.

but depends on the geometry of the magnetosphere) with which the hot continuum flux from the footprint of the magnetosphere is seen through relatively fast moving gas in the accretion stream. The wind component must be very weak. The mass-accretion rate should be much lower ($\dot{M}_{\text{acc}} \sim 10^{-9} \text{ M}_\odot \text{ yr}^{-1}$) than that of the models which produce Type I profiles since the flux in the broadening wings can not be too high to produce the inverse P-Cyg profile.

5.2 Which wind model?

In the previous sections, two possible geometrical configurations for the wind from CTTS were considered: (1) a bipolar wind, and (2) a disc wind. While the material is more concentrated toward the polar regions for a given radius in the first case, the material is more concentrated toward the equatorial plane in the second case.

The distinct difference in the density dependency on the polar angles in two models should be apparent in the inclination angle dependency on the shapes of the line profiles. Figure 18 shows the H α profiles computed for 1. the disc, bipolar-wind, accretion hy-

Table 4. The summary model parameters for the profiles in Figure 17 and brief comments. The temperatures are in 10^3 K. \dot{M}_{acc} and \dot{M}_{dw} are in $M_{\odot} \text{ yr}^{-1}$.

Class	i	\dot{M}_{acc}	T_{max}	\dot{M}_{dw}	T_{dw}	β	Comment
I	55	10^{-7}	7.5	—	—	—	Accretion dominated possibly without the wind. Mid inclination.
II-B	55	10^{-7}	7.5	10^{-8}	8.0	1.0	Wind, disc and magnetosphere. Wide range of wind acceleration rate. Mid–high inclination
III-B	55	10^{-7}	7.5	10^{-8}	9.0	0.5	Wind, disc and magnetosphere. Fast–mid wind acceleration rate. Mid–high inclination
IV-B	55	10^{-7}	7.5	10^{-8}	9.0	0.2	Wind, disc and magnetosphere. Fast wind acceleration rate. Mid–high inclination
II-R	80	10^{-7}	7.5	10^{-8}	7.0	2.0	Wind, disc and magnetosphere. Slow wind acceleration rate. High inclination
III-R	85	10^{-8}	8.2	10^{-9}	6.0	1.0	Wind, disc and magnetosphere. Mid wind acceleration rate. Very high inclination
IV-R	55	10^{-9}	9.5	—	—	—	Accretion dominated. Low mass-accretion rate. Mid inclination.

brid model (section 4.4) and 2. the disc-wind, magnetosphere hybrid model (section 4.5) at inclination angles $i = 10^\circ, 55^\circ$ and 80° . Both models include the magnetospheric accretion component with the same parameters used as in sections 4.4 and 4.5 i.e. $T_{\text{max}} = 7500$ K and $\dot{M}_{\text{acc}} = 1 \times 10^{-7} M_{\odot} \text{ yr}^{-1}$.

Mainly because of the geometrical configuration, the P-Cyg absorption feature weakens as the inclination increases for the model with the bipolar wind. The optical depth to an observer is higher (from the wind emission region) for with a lower inclination angle with this geometry. Although not shown here, this tendency of the inclination dependency holds for the models with bipolar wind models for wide ranges of β and T_{wind} . For the model with the disc wind, the absorption becomes stronger as the inclination becomes larger. The optical depth to an observer becomes larger as the inclination increases in this geometry.

Similarly, the line equivalent width increases as the inclination angle increases for the model with the bipolar wind, it decreases as the inclination angle increases for the model with the disc wind. For the models with only magnetosphere (section 4.1), we find that the line equivalent width decreases as the inclination increases in those models (see Figure 7). Interestingly, the observational study of Appenzeller et al. (2005) showed that the H α line equivalent width of CTTS increases as the inclination angle increases. Only the models with the bipolar wind agree with the trend seen in their observation. Although the uncertainty in the inclination angles of the observed object might be large, a larger sample in addition to that of Appenzeller et al. (2005) for further investigation of the inclination dependency on the line profile will be extremely useful for determining the wind configuration of CTTS.

Despite the inclination angle dependency of the observed H α favouring the models with bipolar wind, there are two main aspects of this model which are not quite consistent with the magneto-centrifugal launched jet numerical models (e.g. Krasnopolsky et al. 2003). First, in section 4.4, we found that the ratio of the mass-loss to mass-accretion rates needed to be rather small ($\mu < \sim 0.025$), in order not to have an unrealistically strong P-Cyg absorption component, compared to the MHD simulations suggested (Königl & Pudritz 2000) i.e. $\mu \approx 0.1$. Considering large uncertainty in MHD theories and observational measurements (e.g. \dot{M}_{acc} , \dot{M}_{wind} and B), the wide range of the mass-loss to mass-accretion ratio may be still reasonable. On the other hand, the models with the disc wind (section 4.5) using $\mu = 0.1$ reproduces the profiles (Figure 16) similar to that seen in observations. Second, the MHD models predict that the wind/jet becomes collimated well above the disc plane (> 10 au), but our bipolar wind model are collimated (density enhanced toward in the polar direction) from right outside of the magnetosphere. Unless the origin of the wind is from the central

star itself, the density distribution used for the bipolar wind is not quite consistent with the near field of the MHD jet models, considering that the most of the H α emission occurs within a few to a several radii of the magnetosphere (Figure 11). The density structure used for the disc wind model, however, is very similar to that of MHD simulations in the near field where the most of the H α wind emission occurs. Interestingly, however, the recent study of Matt & Pudritz (2005) demonstrated the possibility that the stellar wind along the open magnetic field originated from the star can cause significant spin-down torque on the star, provided that mass-loss rate is high enough. Considering the issues mentioned above, it is not possible to favour the bipolar wind model to the disc wind model without further observational constraints. In reality, two types of the winds (bipolar wind and disc wind) may co-exists similar to that seen in e.g. Drew, Proga, & Stone (1998) and Matt & Pudritz (2005). In these models, the fast stellar wind is present in the polar directions, and at the same time the slower disc wind is present near the equatorial plane.

One possible way to distinguish the two different wind models is to examine the profile shape of a CTTS which is known to be viewed at pole-on. If the profile contains a prominent blue-shifted absorption component (e.g. Type IV-B), the system is more likely to be associated with the bipolar wind type of outflow (but not with the disc-wind type of outflow).

6 CONCLUSIONS

We have presented the disc–wind–magnetosphere hybrid radiative transfer models for classical T Tauri stars, and detailed studies of the H α formation from their complex to circumstellar environment to understand the wide variety of H α profiles seen in observations. The two types of wind models considered are (1) the bipolar wind model in which the wind originates from the star itself (section 2.3.1; Figure 1), and (2) the disc-wind model in which the wind originates from the inner part of the accretion disc (section 2.3.2; Figure 3). We found that both wind models combined with the magnetospheric accretion flow reproduces the wide variety of H α profiles (Figures 14 and 16) seen in the observations.

The inclination dependency of the line equivalent width predicted by the bipolar wind model agree with trends seen in the observation, but the disc-wind model does not. With the standard magnetospheric configuration (Table 1), the ratio of the mass-loss to mass-accretion rates (μ) used in the bipolar wind was set to be 4–10 times smaller than that predicated by magneto-hydrodynamical (MHD) calculations (c.f. $\mu \sim 0.1$; Königl & Pudritz 2000) to avoid the blue-shifted absorption component becoming unrealisti-

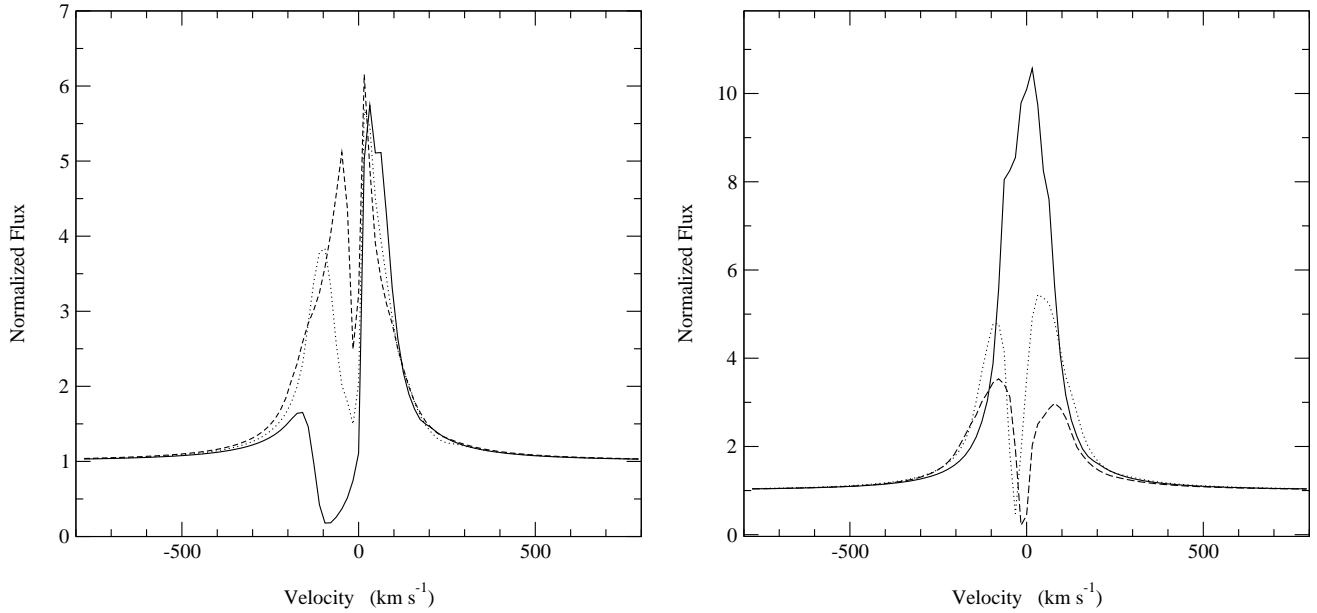


Figure 18. Dependency of the $H\alpha$ model profiles on the inclination angle. The profiles computed at $i = 10^\circ$ (solid), 55° (dot) and 80° (dash) using 1. the disc, bipolar-wind, accretion hybrid model (left panel; c.f. section 4.4) and 2. using the disc-wind, magnetosphere hybrid model (right; c.f. section 4.5) are shown for a comparison. The parameters used for the magnetosphere are same for the both models, i.e. $T_{\max} = 7500$ K and $\dot{M}_{\text{acc}} = 10^{-7} M_{\odot} \text{ yr}^{-1}$. The isothermal wind temperature and the wind acceleration parameter used in both models are $T = 7000$ K and $\beta = 1.0$ respectively. All the other parameters are same as in sections 4.4 and 4.5. While the line equivalent width increases as the inclination angle increases for the former model configuration, it decreases as the inclination angle increases for the latter. Only the former agrees with the tendency seen in the observational study of Appenzeller et al. (2005) who showed that the $H\alpha$ line equivalent width of CTTS increases as the inclination angle increases.

cially too strong; however μ used in the disc-wind models are consistent with MHD calculations.

Using the model results, we examined the $H\alpha$ spectroscopic classification proposed by Reipurth et al. (1996), and discussed the basic physical conditions that reproduce the profiles in each classified type. Using the different combinations of the inclination (i), the mass-loss to mass-accretion rate ratio (μ) and the wind acceleration rate (β), our radiative transfer model was able to produce all 7 types of the profiles in Reipurth et al. (1996).

Similar model configurations used here may be also applicable to Herbig Ae/Be and brown dwarfs since their $H\alpha$ observations also exhibit evidence of the outflow and inflow (e.g. Finkenzeller & Mundt (1984); Muzerolle et al. 2005), but no model has been developed to explain the phenomenon. Further investigation on the possibility of applying our model to these objects are needed.

Future work should include the followings: (1) Improving the wind models. The parametrisation of the wind density structure should be changed to follow more closely that of MHD simulations. The wind temperature structure should be calculated self-consistently (c.f. Hartmann et al. 1994; Martin 1996). (2) Computing the line profiles using the density structure from MHD directly. Check the consistency, and give feedback to the MHD models which are needed to be tested against observational data. (3) Spectropolarimetric study to explore the geometry and the rotation of the disc (e.g. Vink et al. 2005). (4) Modelling of the extended $H\alpha$ and spectro-astrometric observations (c.f. Takami et al. 2003; Appenzeller et al. 2005). (5) Line variability study using a 3D radiative transfer model (e.g. Symington et al. 2005a; Kurosawa et al. 2005) to probe the geometrical structure.

ACKNOWLEDGEMENTS

Authors thank Jorick Vink for providing us the $H\alpha$ data of T Tau. This work is supported by PPARC standard grand PPA/G/S/2001/00081.

References

- Alencar S. H. P., Basri G., 2000, AJ, 119, 1881
- Alencar S. H. P., Basri G., Hartmann L., Calvet N., 2005, A&A, 440, 595
- Anders E., Grevesse N., 1989, geochim. cosmochim. acta, 53, 197
- Appenzeller I., Bertout C., Stahl O., 2005, A&A, 434, 1005
- Appenzeller I., Mundt R., 1989, A&AR, 1, 291
- Bertout C., Basri G., Bouvier J., 1988, ApJ, 330, 350
- Blandford R. D., Payne D. G., 1982, MNRAS, 199, 883
- Burrows C. J., Stapelfeldt K. R., Watson A. M., Krist J. E., Ballester G. E., Clarke J. T., Crisp D., Gallagher J. S., Griffiths R. E., Hester J. J., Hoessel J. G., Holtzman J. A., Mould J. R., Scowen P. A., Trauger J. T., Westphal J. A., 1996, ApJ, 473, 437
- Camenzind M., 1990, Reviews of Modern Astronomy, 3, 234
- Castor J. I., Abbott D. C., Klein R. I., 1975, ApJ, 195, 157
- Castor J. I., Lamers H. J. G. L. M., 1979, ApJS, 39, 481
- Chiang E. I., Goldreich P., 1997, ApJ, 490, 368
- Collier Cameron A., Campbell C. G., 1993, A&A, 274, 309
- Draine B. T., Lee H. M., 1984, ApJ, 285, 89
- Drew J. E., Proga D., Stone J. M., 1998, MNRAS, 296, L6
- Edwards S., Cabrit S., Strom S. E., Heyer I., Strom K. M., Anderson E., 1987, ApJ, 321, 473
- Edwards S., Hartigan P., Ghandour L., Andrus C., 1994, AJ, 108, 1056

- Finkenzeller U., Mundt R., 1984, A&AS, 55, 109
- Frank J., King A., Raine D. J., 2002, Accretion Power in Astrophysics, 3rd edn. Cambridge Univ. Press, Cambridge, p. 398
- Ghosh P., Pethick C. J., Lamb F. K., 1977, ApJ, 217, 578
- Grevesse N., Noels A., 1993, in Origin and Evolution of the Elements, N. P., E. V.-F., M. C., eds., Cambridge Univ. Press, Cambridge, p. 15
- Gullbring E., Hartmann L., Briceno C., Calvet N., 1998, ApJ, 492, 323
- Hanner M., 1988, in NASA Conf. Pub. 3004, 22, Vol. 3004, p. 22
- Harries T. J., 2000, MNRAS, 315, 722
- Hartigan P., Edwards S., Ghandour L., 1995, ApJ, 452, 736
- Hartmann L., Avrett E., Edwards S., 1982, ApJ, 261, 279
- Hartmann L., Hewett R., Calvet N., 1994, ApJ, 426, 669
- Herbig G. H., 1962, Advances in Astronomy and Astrophysics, 1, 47
- Hillier D. J., 1991, A&A, 247, 455
- Johns-Krull C. M., Valenti J. A., Hatzes A. P., Kanaan A., 1999, ApJ, 510, L41
- Kenyon S. J., Hartmann L., 1987, ApJ, 323, 714
- Kenyon S. J., Hartmann L., Hewett R., Carrasco Cruz-Gonzalez I., Recillas E., Salas L., Serrano A., Strom K. M., Strom S. E., Newton G., 1994, AJ, 107, 2153
- Kim S., Martin P. G., Hendry P. D., 1994, ApJ, 422, 164
- Klein R. I., Castor J. I., 1978, ApJ, 220, 902
- Knigge C., Woods J. A., Drew E., 1995, MNRAS, 273, 225
- Königl A., 1991, ApJ, 370, L39
- Königl A., Pudritz R. E., 2000, Protostars and Planets IV, 759
- Krasnopolsky R., Li Z.-Y., Blandford R. D., 2003, ApJ, 595, 631
- Kuhi L. V., 1964, ApJ, 140, 1409
- Kurosawa R., Harries T. J., Bate M. R., Symington N. H., 2004, MNRAS, 351, 1134
- Kurosawa R., Harries T. J., Symington N. H., 2005, MNRAS, 358, 671
- Kurucz R. L., 1979, ApJS, 40, 1
- Long K. S., Knigge C., 2002, ApJ, 579, 725
- Luttermoser D. G., Johnson H. R., 1992, ApJ, 388, 579
- Martin S. C., 1996, ApJ, 470, 537
- Mathis J. S., Rumpl W., Nordsieck K. H., 1977, ApJ, 217, 425
- Matt S., Pudritz R. E., 2005, ApJ, 632, L135
- Mihalas D., 1978, Stellar atmospheres, 2nd edn. W. H. Freeman and Co., San Francisco
- Muzerolle J., Calvet N., Hartmann L., 2001, ApJ, 550, 944
- Muzerolle J., Luhman K. L., Briceño C., Hartmann L., Calvet N., 2005, ApJ, 625, 906
- Ouyed R., Pudritz R. E., 1997, ApJ, 482, 712
- Pudritz R. E., Banerjee R., 2005, in IAU Symposium, pp. 163–173
- Ray T. P., Mundt R., Dyson J. E., Falle S. A. E. G., Raga A. C., 1996, ApJ, 468, L103
- Reipurth B., Pedrosa A., Lago M. T. V. T., 1996, A&AS, 120, 229
- Rybicki G. B., Hummer D. G., 1978, ApJ, 219, 654
- Shakura N. I., Sunyaev R. A., 1973, A&A, 24, 337
- Shang H., Glassgold A. E., Shu F. H., Lizano S., 2002, ApJ, 564, 853
- Shu F. H., Najita J., Ostriker E., Wilkin F., Ruden S., Lizano S., 1994, ApJ, 429, 781
- Symington N. H., Harries T. J., Kurosawa R., 2005a, MNRAS, 356, 1489
- Symington N. H., Harries T. J., Kurosawa R., Naylor T., 2005b, MNRAS, 358, 977
- Takami M., Bailey J., Chrysostomou A., 2003, A&A, 397, 675
- Uchida Y., Shibata K., 1985, PASJ, 37, 515
- Ustyugova G. V., Koldoba A. V., Romanova M. M., Chechetkin V. M., Lovelace R. V. E., 1995, ApJ, 439, L39
- Vernazza J. E., Avrett E. H., Loeser R., 1973, ApJ, 184, 605
- Vink J. S., Drew J. E., Harries T. J., Oudmaijer R. D., Unruh Y., 2005, MNRAS, 359, 1049
- Whitney B. A., Wood K., Bjorkman J. E., Wolff M. J., 2003, ApJ, 591, 1049
- Wood K., Wolff M. J., Bjorkman J. E., Whitney B., 2002, ApJ, 564, 887